

# X-ray properties of protostars in the Orion Nebula

L. Prisinzano<sup>1</sup>, G. Micela<sup>1</sup>, E. Flaccomio<sup>1</sup>, J. R. Stauffer<sup>2</sup>, T. Megeath<sup>3</sup>, L. Rebull<sup>2</sup>, M. Robberto<sup>4</sup>, K. Smith<sup>4</sup>, E. D. Feigelson<sup>5</sup>, N. Grosso<sup>6</sup> and S. Wolk<sup>7</sup>

## ABSTRACT

The origin and evolution of the X-ray emission in very young stellar objects (YSOs) are not yet well understood because it is very hard to observe YSOs in the protostellar phase. We study the X-ray properties of Class 0-I objects in the Orion Nebula Cluster (ONC) and compare them with those of the more evolved Class II and III members. Using Chandra Orion Ultradeep Project (COUP) data, we study the X-ray properties of stars in different evolutionary classes: luminosities, hydrogen column densities  $N_{\text{H}}$ , average plasma temperatures and time variability are compared in order to understand if the interaction between the circumstellar material and the central object can influence the X-ray emission. We have assembled the deepest and most complete photometric catalog of objects in the ONC region from the UV to  $8\mu\text{m}$  using data from the HST Treasury Program, deep and almost simultaneous UBVI and JHK images taken, respectively, with WFI@2.2m ESO and ISPI@4m CTIO telescopes, and *Spitzer* IRAC imaging. We select high probability candidate Class 0-I protostars, distinguishing between those having a spectral energy distribution which rises from K up to  $8\mu\text{m}$  (Class 0-Ia) from those where the SED rises from K up to  $4.5\mu\text{m}$  and decreasing afterwards (Class 0-Ib). In addition, we select a sample of “bona fide” Class II stars and a set of Class III stars with IR emission consistent with normal photospheres.

Our principal result is that Class 0-Ia objects are significantly less luminous in X-rays, both in the total and hard bands, than the more evolved Class II stars with mass larger than  $0.5M_{\odot}$ ; these latter show X-ray luminosities similar to those of Class 0-Ib stars. This result supports the hypothesis that the onset of X-ray emission occurs at a very early stage of star formation and is in agreement with the result found in Giardino et al. (2007). Spectral properties of Class 0-I stars are similar to those of the more evolved Class II and III objects, except for a larger absorption likely due to gas in the envelope or disk of the protostellar objects. Our data suggest that the three different classes have similar X-ray temporal variability.

*Subject headings:* open clusters: general — open clusters: individual (Orion Nebula Cluster) — X-rays: stars — stars: pre-main sequence — stars: activity

---

<sup>1</sup>INAF - Osservatorio Astronomico di Palermo, Piazza del Parlamento 1, I-90134 Palermo, Italy, loredana@astropa.inaf.it

<sup>2</sup>Spitzer Science Center, California Institute of Technology, 1200 East California Boulevard, Pasadena, CA 91125

<sup>3</sup>Department of Physics, University of Toledo, 2801 W. Bancroft Ave, Toledo OH 43606

<sup>4</sup>Space Telescope Science Institute, 3700 San Martin Drive, Baltimore, MD 21218

<sup>5</sup>Department of Astronomy and Astrophysics, Penn State University, 525 Davey Lab, University Park, PA 16802, USA

<sup>6</sup>Observatoire astronomique de Strasbourg, Université

## 1. INTRODUCTION

Young stellar objects (YSOs) exhibit an X-ray luminosity significantly higher than similar stars in the main sequence phase. However, it is still unclear at what stage of their formation process YSOs begin to emit X-rays and how this X-ray emission evolves with time (Favata & Micela 2003;

---

Louis-Pasteur, CNRS, INSU, 11 rue de l'Université, 67000 Strasbourg, France

<sup>7</sup>Harvard Smithsonian Center for Astrophysics, MS 65, 60 Garden Street, Cambridge, MA 02138

Feigelson et al. 2007).

Evidence has accumulated over the past few years that among the YSOs, the X-ray luminosity function (XLF) of Classical T Tauri stars (CTTS) is different from that of Weak T Tauri stars (WTTS). Such a difference has been investigated by some because the accretion and outflow processes, characteristic of the CTTS phase, involve the interaction of ionized material with the star and disk magnetic field, and these media play a fundamental role in the coronal X-ray emission of young stars. Using the *Chandra* Orion Ultradeep Project (COUP) data (Getman et al. 2005b), Preibisch et al. (2005) find that the accreting stars, as discriminated using the CaII 8542Å IR triplet line, are less X-ray luminous than non-accretors, while no differences are found for stars with  $(K - L)$  IR excesses, indicative of the presence of a (possibly passive) disk, with respect to stars without IR excesses. These results are in agreement with those found in the previous work in the ONC by Flaccomio et al. (2003b,c) who found a strong difference in the X-ray luminosity of accreting and non-accreting stars.

In order to understand the evolution of the X-ray emission during the star formation process, Preibisch & Feigelson (2005) looked for a possible relation between X-ray emission and stellar age in the ONC. They found, in the age range  $\sim 0.1 - 10$  Myr, a slow decay in the X-ray luminosity,  $L_X$ . Because, as the star contracts, the bolometric luminosity,  $L_{bol}$ , decreases faster than  $L_X$ , on average  $L_X/L_{bol}$  and the X-ray surface flux,  $F_X$ , increase during this age range.

In this work, we want to investigate the onset and the evolution of X-ray emission during the early phase of the star formation by statistically comparing the X-ray properties of the stars in different evolutionary phases rather than considering individual stellar ages, usually derived from theoretical isochrones. We hope in this way to avoid some of the problems introduced when using inferred ages (due to their often large random and systematic uncertainties; see, e.g., Hillenbrand et al. 2007).

YSOs in their early phases are characterized by IR excesses due to the presence of a circumstellar envelope and/or a disk that contains warm dust. The first IR classification in Class I, II and III sources, which is based on the IR spectral in-

dex, was proposed by Lada (1987). The discovery in the sub-mm of cold objects, younger than the IR sources, leads to the introduction of the Class 0 sources (Andre et al. 1993). Based on their mid-IR properties, YSOs are usually classified as follows (e.g. Allen et al. 2004; Megeath et al. 2004; Lada et al. 2006; Allen et al. 2007): Class 0 objects are protostars surrounded by the initial infalling envelope, typically detected in the sub-millimeter and far-IR; Class I objects are evolved protostars surrounded by an envelope and a circumstellar disk; Class II stars are objects with a circumstellar disk but lacking significant evidence for a dense envelope and finally Class III stars are objects that have lost their initial envelope and disk and show optical and near-IR colors consistent with normal photospheres. By providing very sensitive 3.6-70  $\mu\text{m}$  data with good angular resolution, *Spitzer* observations have provided a much better census of the stellar populations in a number of star-forming regions. However, *Spitzer* data have also complicated the YSO classification system, allowing detection of some Class 0 objects at wavelengths as blue as 3.6  $\mu\text{m}$ .

Our intent is to compare the X-ray properties of protostars - where to date there are relatively few studies - with the X-ray properties of the more evolved Class II and III stars, for which the X-ray emission is well studied. Such a comparison is fundamental in order to understand the onset of X-ray emission in YSOs and its evolution in the early phases of star formation.

Previous studies of X-ray emission from Class 0-I objects include Ozawa et al. (2005), who studied core F of the  $\rho$  Ophiuchi cloud and found a high X-ray detection rate (64%) of Class I sources. They suggest that an evolutionary effect in temperature and extinction is present from Class I to Class III stars, these latter having lower coronal temperatures and extinction.

A similar result has also been found by Giardino et al. (2007). Getman et al. (2007) studied the IC 1396N cometary globule where they found 6 X-ray emitting protostars, including the Class 0-I IRAS 21391+5802 which they claim to be one of the youngest objects ever detected in X-rays. The comparison of X-ray emission from different evolutionary classes is, however, hampered by the difficulty of detecting X-rays from Class 0 protostars. For example, no X-ray emission has been

found from Class 0 stars in the Serpens, one of the most sensitive surveys (Giardino et al. 2007), even if important detections have been found in other surveys (e.g. Tsuboi et al. 2001; Hamaguchi et al. 2005; Tsujimoto et al. 2005; Getman et al. 2007).

The ONC is a prime target for this kind of investigation. It is the nearest concentrated site of star formation with a very large number of known members covering all evolutionary stages. It is the best studied region at all wavelengths, in particular, in the X-ray band. Many interesting results have been obtained with the extraordinarily long *Chandra* observation performed by the COUP project. To understand the evolution of X-ray activity from the very first stages of the star formation process, it is necessary to distinguish Class 0-I objects from Class II stars. Such a classification, based on the shape of the spectral energy distribution (SED) is not available in the literature and requires complete and deep near and mid IR data.

We present here the results of the X-ray study of YSOs in the ONC classified using the *Spitzer* IRAC catalog (Megeath et al. 2005), groundbased JHK data (Robberto et al. 2007, in preparation) and the deep photometric catalog obtained within the HST Treasury Program (Robberto et al. 2005b). Using the COUP data, we have studied the X-ray properties of YSOs from their initial protostellar phase (Class 0-I objects) to the more evolved pre-main sequence (PMS) stage of no longer accreting and disk free stars (Class III objects). We have classified the ONC members using conservative criteria in order to minimize the contamination of the resulting samples. Because of the large area coverage and the richness of the ONC, we have obtained an homogeneous and statistically significant sample of X-ray detected Class 0-I objects. We are thus able, for the first time, to compute the X-ray luminosity function (XLF) of Class 0-I stars and to compare it with the XLF of Class II and III stars.

## 2. OBSERVATIONS

We have assembled a deep photometric catalog of the ONC from the UV to  $8\mu\text{m}$  obtained using new optical/NIR observations taken within the HST Treasury Program (Robberto et al. 2005b), using a variety of telescopes and detectors, and *Spitzer* IRAC (Werner et al. 2004;

Fazio et al. 2004) imaging. The optical photometry was derived using images taken with the Wide-Field Planetary Camera 2 (WFPC2) of HST (Robberto et al. 2005b) and with the Wide Field Imager (WFI) at the ESO 2.2m Telescope (Robberto et al. 2007, in preparation). *JHK* photometry was obtained from images taken with the Infrared Side Port Imager (ISPI) camera at the CTIO Blanco 4m telescope (Robberto et al. 2007, in preparation). *Spitzer* IRAC photometry in the four standard filters centered on 3.6, 4.5, 5.8 and  $8.0\mu\text{m}$  was obtained by Megeath et al. (2005). A detailed description of the optical-IR observations is given in Table 1. We note that the magnitude limits given in this table are typical values for each survey. However, due to the complex structure of the nebulosity in the ONC (and due to varying integration times for different parts of the region), the sensitivity is not uniform. For example the limiting magnitude at  $3.6\mu\text{m}$  is about 16 within most of the COUP FOV, while it is about 10 within a region of  $1'$  in radius around the brightest stars of the Trapezium cluster.

### 2.1. X-ray data

X-ray data used in this work were obtained with the  $\sim 838$  ks COUP observation of the ONC, taken with the ACIS camera that covers a FOV of  $17' \times 17'$ . Details of data reduction and the derived catalog of 1616 sources can be found in Getman et al. (2005b).

### 2.2. Optical data

New optical photometric data taken with the WFPC2 camera of HST were used by Robberto et al. (2005b) to derive the optical photometric catalog used in this work. This catalog contains 1754 selected point sources with at least a detection in the F814 band.

The recent HST survey has been complemented with UBVI images taken with the WFI camera of the ESO 2.2m Telescope. Details on data reduction and photometric catalog derivation will be described in Robberto et al. (2007, in preparation). This catalog contains 2744 selected point sources with at least a detection in the I band.

Additional optical data were retrieved from literature including the catalogs of Hillenbrand (1997, hereafter H97), Rebull et al. (2000) and

Table 1: Log of the new optical-IR observations used in this work.

Nights	Telescope	Camera	Filters	Exp. time <sup>a</sup> [sec]	Mag. Lim. <sup>b</sup>	Field of view	Reference
2006 May	HST	WFPC2	F336W <sup>c</sup>	2×400	F336W $\simeq$ 20.0	30'×30'	1
2006 May	HST	WFPC2	F439W <sup>c</sup>	80	F439 $\simeq$ 20.7	30'×30'	1
2006 May	HST	WFPC2	F656N <sup>c</sup>	400	F656N $\simeq$ 18.0	30'×30'	1
2006 May	HST	WFPC2	F814W <sup>c</sup>	10	F814 $\simeq$ 20.0	30'×30'	1
2005 Jan. 1-2	ESO 2.2 m	WFI	U, B, V, I <sub>c</sub>	3, 30, 280	I <sub>c</sub> $\simeq$ 21.7	35'×34'	2
2005 Jan. 1	CTIO Blanco 4m	ISPI	J, H, K <sub>s</sub>	3, 30	K <sub>s</sub> $\simeq$ 18.7	6×(10':25×10':25)	2
2005 Jan. 2	CTIO Blanco 4m	ISPI	J, H, K <sub>s</sub>	3, 30	K <sub>s</sub> $\simeq$ 18.7	8×(10':25×10':25)	2
	<i>Spitzer</i> <sup>d</sup>	IRAC	(3.6, 4.5, 5.8, 8.0) $\mu$ m		[3.6] $\simeq$ 16.8	5.6 sq. degrees	3

<sup>a</sup>Exposure time per filter

<sup>b</sup>Magnitude limit computed for stars with photometric errors smaller than 0.1

<sup>c</sup>WFPC2 filters F336W, F439W, F656N, F814W corresponds to the standard filters U, B, H $\alpha$  and I, respectively

<sup>d</sup>Data part of the *Spitzer*/GTO Programs 43 and 50 taken in high dynamic range mode using 0.6 and 12 sec at each position.

References. — (1) Robberto et al. (2005b); (2) Robberto et al. (2007) in preparation; (3) Megeath et al. (2005)

Herbst et al. (2002).

### 2.3. *JHK* data

The *JHK* photometric catalog has been obtained using images taken with the ISPI camera at the CTIO Blanco 4 m Telescope. Details on data reduction and photometry will be given in Roberto et al. (2007, in preparation). The survey includes a mosaic of 11 fields, each of  $10'.25 \times 10'.25$ , centered around the Trapezium cluster. All fields were observed once using a 5 point dithering pattern. From the source catalog we excluded saturated objects, that is, those with a peak flux in each band higher than 37000 counts and entries with errors in magnitudes larger than 0.2. After this selection, we were left with 17824 entries in the table.

Finally, we constructed a consolidated catalog of individual objects by merging entries with positions within  $0''.6$ , the radius at which spurious identifications start to dominate. For each object, we computed the mean coordinates and magnitudes. Our final *JHK* photometric catalog contains 13987 objects.

Additional *JHK* data were retrieved from the 2MASS catalog (Cutri et al. 2003).

### 2.4. *Spitzer* IRAC data

A description of the data, the reduction procedure and the derived photometric catalog obtained from the *Spitzer* IRAC images is given in Megeath et al. (2005). The survey covers the Orion A and B molecular clouds for a total of 5.6 sq. degrees with a sensitivity of 17.0, 16.0, 14.5 and 13.5 mag in the  $3.6 \mu\text{m}$ ,  $4.5 \mu\text{m}$ ,  $5.8 \mu\text{m}$  and  $8.0 \mu\text{m}$  bands, respectively. The uncertainties in the calibration are about 5%, but for a few stars are significantly worse due to the bright nebulosity in the 5.8 and  $8.0 \mu\text{m}$  bands. Within the region studied in this work, i.e. the COUP FOV, the catalog includes 1244 sources detected both at  $3.6 \mu\text{m}$ ,  $4.5 \mu\text{m}$  and 334 sources detected both at  $5.8 \mu\text{m}$ ,  $8.0 \mu\text{m}$ . The *Spitzer* Orion Survey also included MIPS observations at  $24 \mu\text{m}$  that we do not use in the following analysis since they are saturated in the COUP region due to the high background from the HII region.

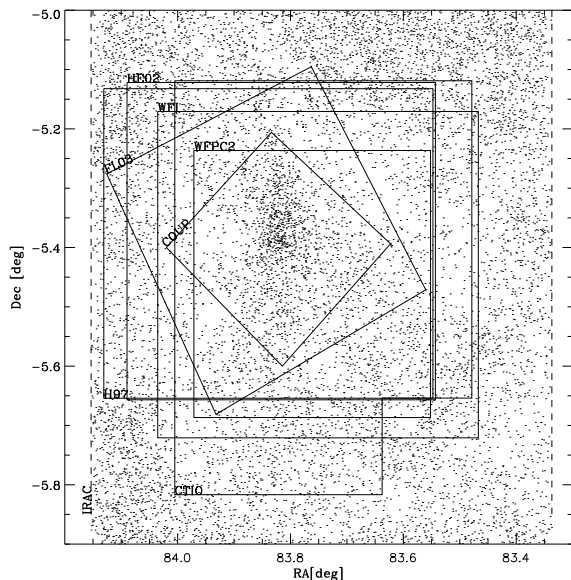


Fig. 1.— The field of view (FOV) of the catalogs considered in this work are overplotted on the spatial distribution of the stars detected with IRAC. Note that the FOV of the IRAC (dashed line), Rebull et al. (2000) and 2MASS data (not indicated here) are larger than the field shown in this figure.

## 2.5. Cross identifications of sources

All the photometric catalogs obtained from the observations described in Table 1 were assembled in a single database. Common objects between two catalogs were found using the nearest neighbour method by first considering two sources as the same object if their positions agree to within a specified amount -  $1''$ - $3''$ - depending on the absolute astrometric accuracy of the catalogs. Matched sources were then used to compute the median and the standard deviation of the offsets. These median values were used to remove the systematic offsets between each pair of matched catalogs, and new matches were performed, for all pairs of catalogs, using new tolerances computed using the standard deviation of the offsets.

Using the same matching procedure we have cross-correlated these data with the literature catalogs of Hillenbrand (1997), Rebull et al. (2000), 2MASS (Cutri et al. 2003), Herbst et al. (2002), Muench et al. (2002) and the X-ray source list from the COUP Survey (Getman et al. 2005b).

Finally we collected all data from all the cross-matched catalogs, including all objects detected in at least one catalog.

The field of view (FOV) covered by these surveys are overplotted in Fig. 1 on the spatial distribution of the stars detected with IRAC around the ONC. Note that the FOV of the IRAC, Rebull et al. (2000) and 2MASS data (not indicated) are larger than the field shown in the figure.

Since this work is focused on the X-ray properties of the young stars in the ONC, only stars within the COUP FOV will be considered in the following analysis. In addition, photometric data with errors smaller 0.2 mag will be considered.

## 3. YSO CLASSIFICATION

In this Section we describe how we select ONC stars belonging to the three different evolutionary classes 0-I, II and III. Our approach is to select conservative, even if incomplete, samples in order to be able to compare the X-ray properties of the stars in different evolutionary stages using samples that are as “uncontaminated” as possible.

### 3.1. Class 0-I protostars

According to Lada & Wilking (1984) and Adams et al. (1987), the first stage of YSO evolution is the infall phase around a central protostar undergoing accretion, characterized by strong emission in the sub-millimeter and far-infrared and weak emission shortward of  $24 \mu\text{m}$ . These objects, indicated as Class 0, can have outflows and are defined as protostars with half or more of their mass in the envelope. More evolved protostars are the Class I objects with both a disk and envelope surrounding the central star. Both these classes of protostars are characterized by a steeply rising SED in the infrared range, although pure Class 0 objects are expected to be fainter at near and mid-IR bands (Allen et al. 2007).

Since our data extend only to  $8 \mu\text{m}$ , we cannot distinguish between Class 0 and Class I stars and we will combine them into one group as Class 0-I protostars; we classify them using the following criterion: we computed  $\log(\lambda F_\lambda)$  over the wavelengths  $[\lambda_1, \dots, \lambda_5] = [2.2, 3.6, 4.5, 5.8, 8.0] \mu\text{m}$ , i.e. the K-band and the four IRAC bands with the Lada et al. (2006) flux conversion factors that are in agreement with the Reach et al. (2005) values; for each star we then computed the slopes for each pair of adjacent bands

$$\frac{\log(\lambda_{i+1} F_{\lambda_{i+1}}) - \log(\lambda_i F_{\lambda_i})}{\log \lambda_{i+1} - \log \lambda_i} \quad \text{for } i = 1, 4;$$

we consider Class 0-I objects those for which the slopes are all larger than 0, i.e. objects with rising SEDs. This criterion is more conservative than using the single slope (usually indicated as spectral index) computed from the linear fit of the  $\log(\lambda F_\lambda)$  function over the whole wavelength range, because it only selects monotonically increasing SEDs. Moreover, it is more robust than those based on only a color-color diagram (CCD) since it is based simultaneously on all the known magnitudes.

Our sample of Class 0-I objects includes all the objects for which we have at least three of the five magnitudes and therefore at least two slopes. This allows us to include objects detected only in the K,  $3.6 \mu\text{m}$  and  $4.5 \mu\text{m}$  bands but not at  $5.8$  &  $8.0 \mu\text{m}$ ; because of the bright nebular background and the lower sensitivity at  $8 \mu\text{m}$ , many objects are not detected in these two bands (roughly 44% of the Class 0-I sample).

Using this criterion, we end up with 41 potential Class 0-I objects in the COUP field of view (Getman et al. 2005b). Eighteen of them have a detection in at least one of the optical UBVI bands. Since protostars are expected to be heavily embedded and therefore highly reddened objects, we do not expect to detect them in the visible. Of these 18 peculiar objects, 5 (COUP # 693, 747, 826, 948, 1011) are in the list of the X-ray detected proplyds given in Kastner et al. (2005). From a visual inspection of ACS/HST images, we conclude that all 18 of these objects have a counterpart in the HST optical bandpasses, while the other 23 objects are not detected at these bands. We eliminate these 18 objects from our list of candidate Class 0-I stars and we consider the remaining 23 stars as Class 0-Ia objects to distinguish them from the additional sample of candidate Class 0-I described below. The SEDs of the 23 selected Class 0-Ia stars are plotted in Fig. 2. The photometry is given in Table 5 where Column 1 gives the sequential number in our catalog, Column 2 is the COUP identification number, Columns 3 and 4 are the J2000 coordinates, Columns 5 to 11 give the JHK and IRAC magnitudes. Of these 23 objects, 10 (~40%) have an X-ray counterparts in the COUP data. One of these (COUP # 702) is in the Getman et al. (2005a) list of nonflaring COUP X-ray sources without optical and NIR counterpart and was flagged by them as a probable extragalactic object (EG).

Fig. 3 shows the color-color diagrams (CCDs) obtained using the K and IRAC magnitudes of all the stars in the COUP field of view. The plot on the left panel includes more stars than those on the central and right ones because it does not require detections at 5.8 and 8.0  $\mu\text{m}$ . The limited sensitivity of the 8.0  $\mu\text{m}$  channel means that few objects with zero color (consistent with photospheric emission) appear in the right panel. The selected Class 0-Ia objects with increasing SED, indicated in Fig. 3 by squares, show  $[3.6]-[4.5]>0.7$  and  $[5.8]-[8.0]\gtrsim 1.1$ . The objects with  $[3.6]-[4.5]>0.7$  and  $[5.8]-[8.0]\lesssim 1.1$  that are usually also classified as Class 0-I stars (Allen et al. 2004; Megeath et al. 2004), show a decreasing or flat SED at wavelengths longer than 4.5  $\mu\text{m}$ . The spectral energy distributions of protostars in this spectral regime are complex as rotation (Kenyon et al. 1993) and outflow cavities (Whitney et al. 2003)

reduce the extinction toward the poles of the protostellar envelopes allowing radiation to leak and scatter out. Consequently, protostars can also exhibit decreasing slopes, particularly between 4.5 and 8.0  $\mu\text{m}$ , depending on their inclination (Whitney et al. 2003). Furthermore, highly reddened Class II objects can have increasing slopes; however, these slopes will generally flatten or decline for  $\lambda \geq 4.5\mu\text{m}$  due to the flattening of the reddening law and the broad silicate feature at 9.7  $\mu\text{m}$  (Flaherty et al. 2007). Thus, although the IRAC data can enhance the identification of protostars by extending the SEDs to 8 microns; establishing a sample of protostars uncontaminated by reddened Class II objects is still difficult without photometry at wavelengths  $\lambda > 8 \mu\text{m}$ .

To take into account these cases, we also include the objects with a decreasing SED for  $\lambda > 4.5\mu\text{m}$  in our Class 0-I sample. There are 28 such objects in total. After rejecting the six objects with optical counterparts in the HST imaging, we are left with 22 objects, which we refer to hereafter as Class 0-Ib sources. The SEDs of the Class 0-Ib objects are shown in Fig. 4, while the photometry is given in Table 6, analog to Table 5. Among these objects, 18 (~80%) are in the COUP list of X-ray detection, including COUP source 1565, which was classified as an extragalactic object by Getman et al. (2005a).

If we consider both Class 0-Ia and Class 0-Ib samples, our list of X-ray detected Class 0-I objects (10+18) is one of the largest sample of Class 0-I stars with evidence of X-ray emission (Getman et al. 2007; Giardino et al. 2007).

Our selected Class 0-I objects fall in the region of the envelope models indicated in Allen et al. (2004) and Megeath et al. (2004). There are a small number of objects falling in the Class 0-I regions of the CCD which were not selected with our criterion because either they have an optical counterpart (18+6 in total) or their SED band-to-band slopes do not increase as required by our criterion. Whereas some of these rejected objects could be Class 0-I stars, by adopting a conservative selection criterion, we have minimized the adverse effect of sample contamination for our comparison of X-ray properties.

A careful examination of the near-IR and IRAC colors of our Class 0-I candidates (see Figs. 3 and 5) suggests to us that the Class 0-Ia's (on average)

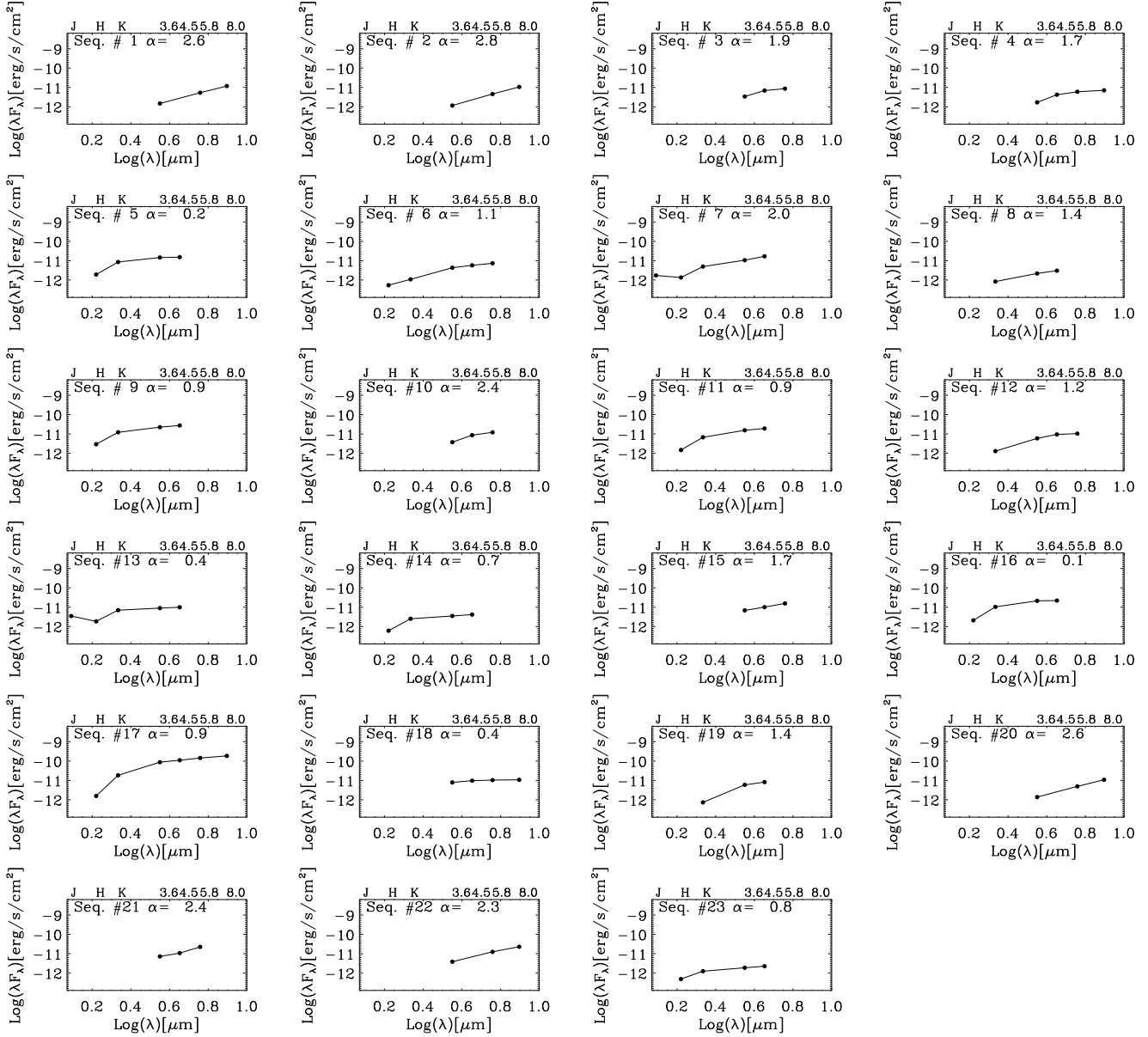


Fig. 2.— SED of the 23 Class 0-Ia candidate objects with a rising SED from K to 8.0 μm. The sequential number in our catalog and the spectral index computed using the available IRAC magnitudes are also indicated.

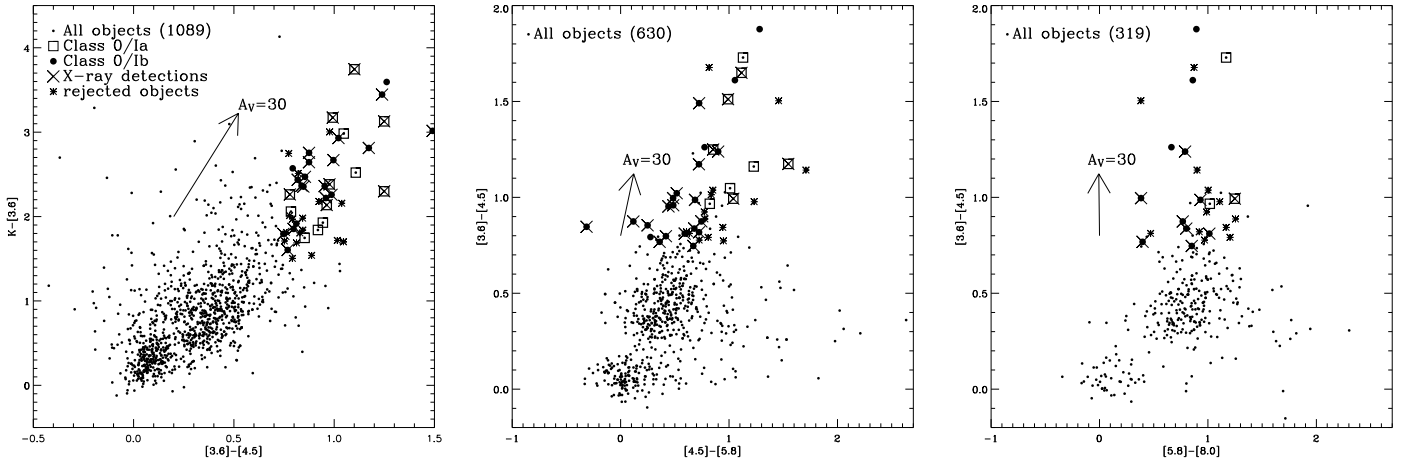


Fig. 3.— CCD of the stars in the COUP field of view (dots) created using the  $K$  and the *Spitzer* IRAC magnitudes. The total number of objects in each diagram is reported in the three panels. Squares and large filled circles represent the Class 0-Ia and 0-Ib objects, respectively, while X symbols indicate those with an X-ray counterpart; asterisks indicate objects rejected because they have an optical counterpart. The reddening vectors computed using the IR reddening law given in Flaherty et al. (2007) for Orion A are also plotted.

are inconsistent with their being heavily reddened Class II's. In particular, the bottom-right panel of Figure 5 shows that, using the Orion A reddening law of Flaherty, the Class 0-Ia's are too red in  $[4.5]-[5.8]$  to be heavily reddened Class II's - and in any case would require reddenings of  $A_V \geq 60$ . The bottom left panel of Fig. 5 also indicates that the Class 0-Ia's, on average, would need very large reddenings ( $A_V \sim 50$ ) for them to be Class II sources. Such heavily embedded objects would likely be very young in any case - and we therefore believe it is more likely that they are, indeed, Class 0 or Class I objects. By contrast, the Class 0-Ib objects are located in all of the diagrams in Figs. 3 and 5 in positions consistent with being moderately reddened ( $A_V \sim 30$  on average) Class II's. We suspect the Class 0-Ib's are a mixture of true Class 0 or I objects, and heavily reddened Class II's - without more data we cannot clean the sample any further than we have.

Another possible worry is that our Class 0-I candidate sample includes systems seen edge-on in or around the HII region. In these cases, relatively evolved Class II objects may display a SED peaking at mid-IR and far-IR wavelengths, as suggested by Robberto et al. (2002). However, since edge-on disks should be randomly distributed in

the nebula, clustering in the dark regions of the selected objects (see Fig. 6a) strongly suggests that they are real protostars.

### 3.2. Class II stars

Following Hartmann et al. (2005), Class II objects within the COUP field of view were selected using the condition  $0.2 < [3.6] - [4.5] < 0.7$  and  $0.6 < [5.8] - [8.0] < 1.1$ . These criteria are slightly more restrictive than those adopted by Megeath et al. (2004) in order to attempt to create as "pure" a set of Class II's as possible. With our selection criteria, we may lose reddened Class II objects, but assuming that X-ray properties of Class II stars are independent of their reddening, our sample should be representative of the Class II population.

Using this criterion, we find 148 Class II stars with NIR photometry given in Table 7, analogous to Table 5; 130 of these objects (about 88%) are X-ray detected. One of them, the COUP source 1401, is listed by Getman et al. (2005a) as a flaring source and classified as an Orion Molecular Core (OMC) member, whereas another Class II object, COUP source 751, was classified by the same work as extragalactic object. Among the 130

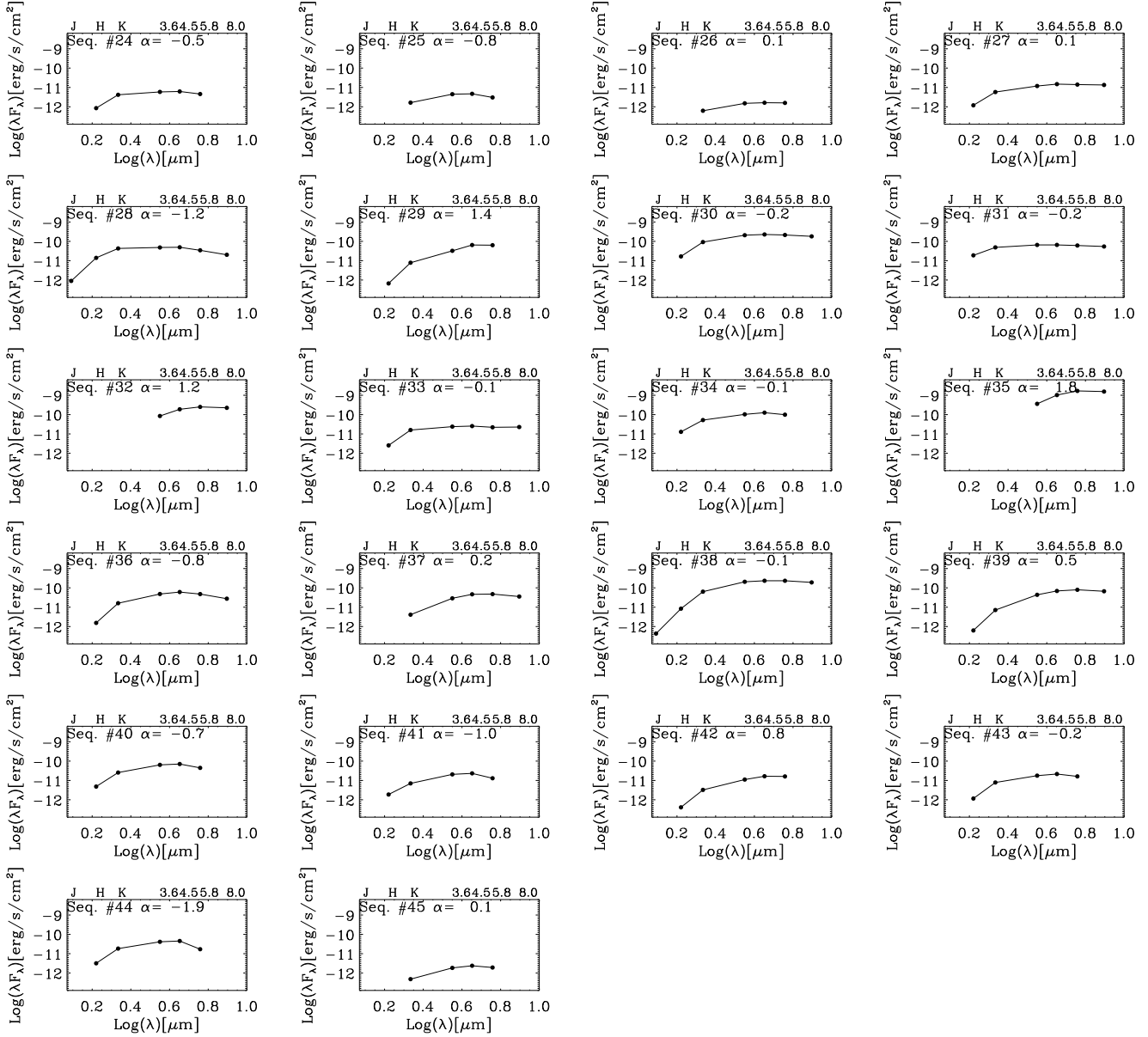


Fig. 4.— SED of the 22 Class 0-Ib candidate objects with a rising SED from K to 4.5  $\mu\text{m}$ . The sequential number in our catalog and the spectral index computed using the available IRAC magnitudes are also indicated.

X-ray detected Class II stars with a counterpart in the Hillenbrand (1997) catalog, 83 have a measure of the equivalent width of the Ca II 8542Å line  $W(\text{Ca II})$ . Among these, 28 have  $W(\text{Ca II}) < -1$ , which is the limit used by Flaccomio et al. (2003a) to classify strong accretors. Therefore we have about 55 objects (i.e.  $\sim 66\%$ ) that have a near-IR bright inner disk but relatively low accretion rate. Of the 148 Class II stars we have identified, we will consider in the following analysis only the 87 X-ray detected and the 9 X-ray undetected stars for which masses are known (Hillenbrand 1997; Getman et al. 2005b). We retain only these stars in order to study the X-ray properties as a function of stellar mass.

### 3.3. Class III stars

Class III objects are PMS stars that do not show IR excesses and therefore were selected as those having IRAC colors near zero. In order to include all the stars not detected in the longer wavelength IRAC bands, we selected all the stars with  $K - [3.6] < 0.5$  and rejected those with  $[3.6] - [4.5] > 0.2$  or  $[4.5] - [5.8] > 0.2$  or  $[5.8] - [8.0] > 0.2$ , when these latter colors were available, i.e. objects with IR excesses. Stars undetected in the IRAC bands at wavelengths longer than  $3.6 \mu\text{m}$  were included since their non-detection in these bands is compatible with purely photospheric SEDs.

Using these criteria, we selected 205 objects, with photometry given in Table 8; 160 of them (about 80%) have an X-ray counterpart. Among these latter, 150 are in the list of Hillenbrand (1997). In particular, 130 of them have a proper motion membership probability larger than 90%, 6 have a membership probability equal to 0 and the other 14 have no membership probabilities. For the remaining 10 stars without a counterpart in the list of Hillenbrand (1997), X-ray detection is the only known membership criterion. We note that none of these 10 objects is either in the list of flaring or in that of non-flaring sources of Getman et al. (2005b). Therefore the membership class for these objects remains uncertain.

Of the 45 objects without an X-ray detection, 18 have a counterpart in the Hillenbrand (1997) catalog but only 5 of these have a proper motion membership probability larger than 90%.

The remaining 40 objects without a mem-

bership criterion could be either Class III stars without X-ray activity, or field stars. Of the 205 Class III stars initially selected, we will consider the 103 X-ray detected stars for which the mass is known (Getman et al. 2005b) and with Hillenbrand (1997) membership probability larger than 90%; in addition, from the sample of X-ray undetected Class III candidates, we will retain only the 2 objects with membership probability larger than 90% and for which a mass has been derived by Hillenbrand (1997).

Fig. 5 shows the selected stars in the IRAC CCD and color-magnitude diagrams. These diagrams show that our samples of YSOs most likely do not include AGN or star-forming galaxies; that is, they do not include objects falling in the wedge-shaped regions outlined in the upper panels of Fig. 5. Star-forming galaxies are usually dominated by PAH features in the 5.8 and  $8.0 \mu\text{m}$  and therefore have  $[5.8] - [8.0] > 1.0$  but  $[3.6] - [4.5] \lesssim 0.3$ , that corresponds to the regions indicated by solid lines in the two upper panels of Fig. 5 (Gutermuth et al. 2007). AGN, instead, have  $[3.6] - [4.5]$  and  $[5.8] - [8.0]$  colors very similar to the Class II YSOs, but are typically much fainter than YSOs, having, for example,  $[4.5]$  magnitudes (Megeath et al. 2005), much fainter than those of the selected YSOs (see bottom-left panel in Fig. 5).

## 4. SPATIAL DISTRIBUTION

The spatial distribution of YSOs within the molecular cloud from which they have formed may give important clues for understanding the star formation process. Using the classification defined in the previous section, we have analyzed the spatial distribution of the YSOs in the ONC, as shown in Fig. 6a where we plot the position of all 2590 objects in our catalog within the COUP field of view that have been detected in at least two of the UBVIJHK and IRAC bands and the Class 0-I candidates. Stars of Class II and III are plotted in Fig. 6b and c, respectively.

Figure 7 shows the velocity integrated  $^{13}\text{CO}$  map obtained by Bally et al. (1987) and the *Spitzer* IRAC image at  $3.6 \mu\text{m}$  where the different classes selected in this work have been overplotted. The upper green box indicates a  $40'' \times 50''$  region around the Becklin-Neugebauer

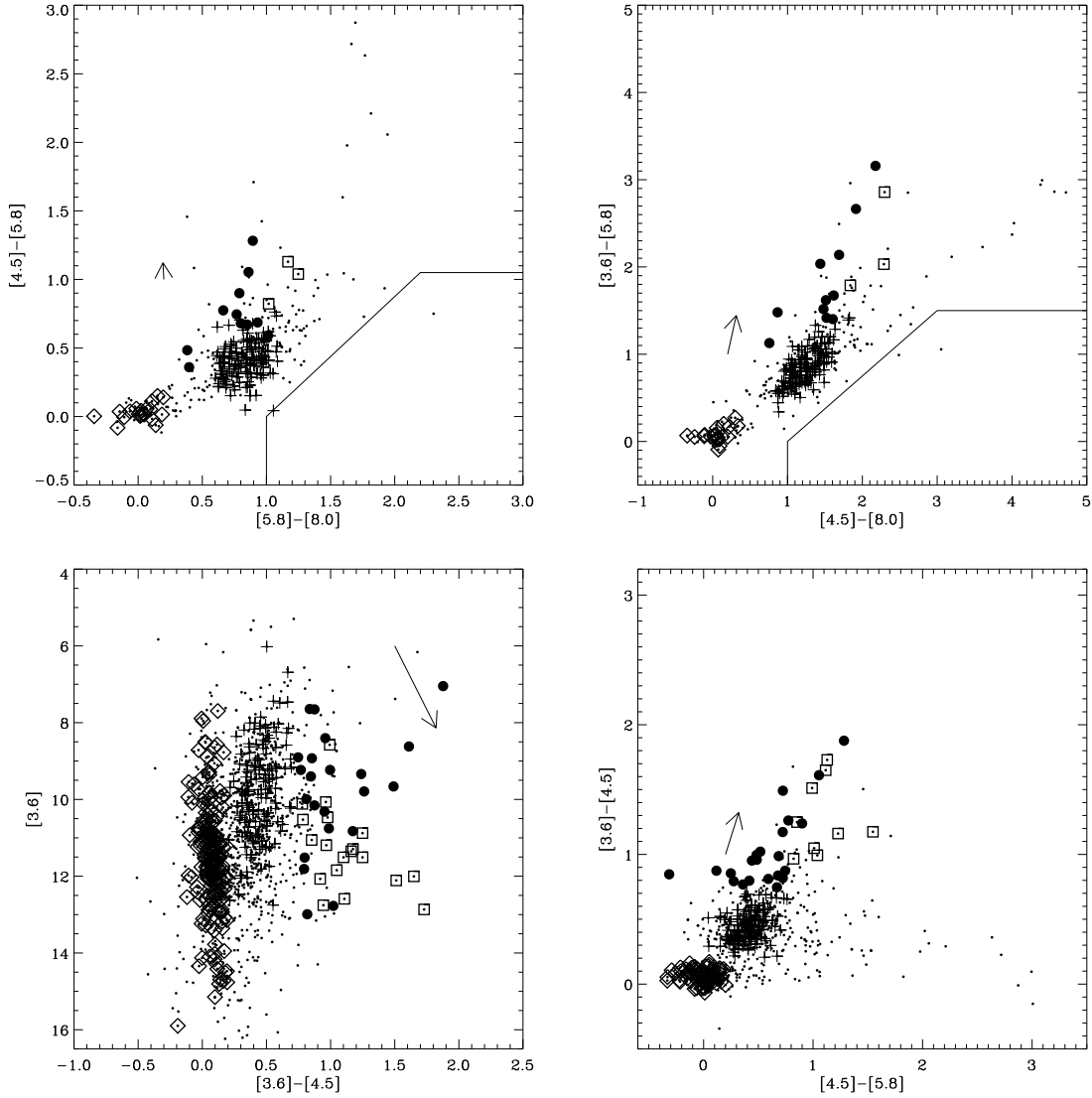


Fig. 5.— IRAC CCD and color-magnitude diagrams of the different populations in the ONC. Dots indicate all the stars in the COUP field of view with detections at the bands used in each panel. Squares and large filled circles are the Class 0-Ia and 0-Ib objects, respectively, plus symbols are the stars classified as Class II and diamonds are the Class III stars. The reddening vector corresponding to  $A_V = 30$ , computed using the Flaherty et al. (2007) reddening law, is plotted on each panel. The solid lines in the above panels separate the region dominated by YSO's from the region expected to be dominated by galaxies.

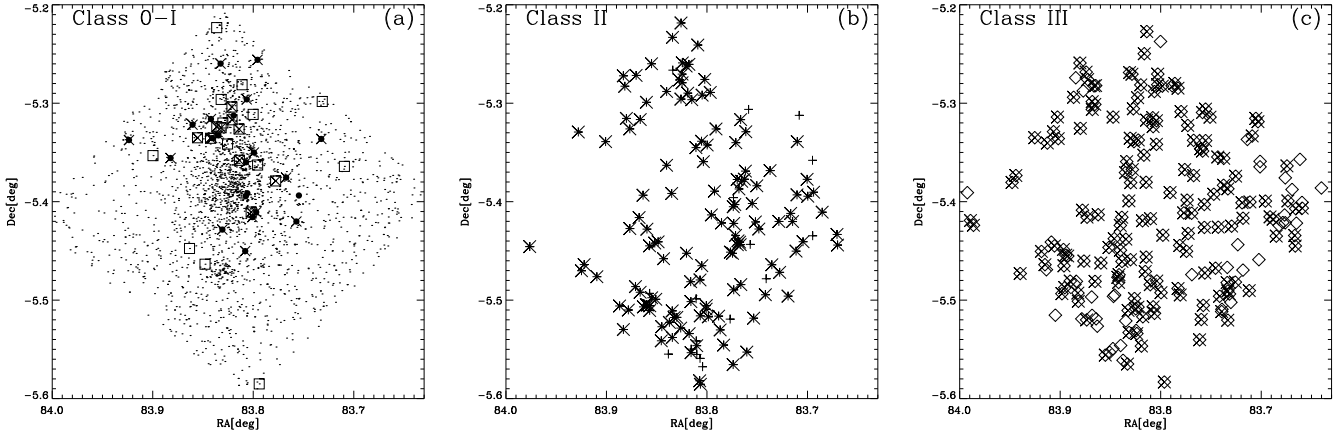


Fig. 6.— Spatial distribution of all the objects in our catalog within the COUP field of view that have been detected in at least two of the UBVJHK and IRAC bands. Squares and large filled circles indicate Class 0-Ia and 0-Ib objects, plus symbols the Class II stars and diamonds the Class III objects. In all the panels, X-ray detected objects are indicated with an X symbol.

object and the Kleinmann nebula, also indicated as BN-KL ( $RA_{2000}=05^h35^m14^s16$ ,  $Dec_{2000}=-05^{\circ}22'21.5''$ ). The bottom green box indicates a  $60'' \times 75''$  region around the Orion Molecular Cloud 1 (OMC-1S) ( $RA_{2000}=05^h35^m14^s50$ ,  $Dec_{2000}=-05^{\circ}25'49.0''$ ). These boxes show the limits of the areas studied in Grosso et al. (2005).

Most of the Class 0-I stars are concentrated in the central and north-east parts of the COUP field of view along a region running north-south from the Trapezium that follows the north-south distribution of the  $^{13}\text{CO}$  emission, i.e. of the dense star-forming gas. The distribution of our selected Class 0-I objects is biased by our NIR observations which are more sensitive towards the north of the molecular ridge where the nebular contribution is lower. The lack of Class 0-I objects in the BN-KL and OMC-1s regions is due to the bright nebulosity, as is evident from the image at  $3.6\ \mu\text{m}$ , that causes a decrease of sensitivity in the central region. For this reason, the spatial distribution of our Class 0-I objects cannot be directly compared with that obtained by Lada et al. (2000, 2004), although in fact the two spatial distributions are quite similar.

Figures 6 and 7 show the same structure already found in Feigelson et al. (2005) using the lightly X-ray absorbed stars: they interpreted this distribution as due to a process of violent relaxation.

Note that, the latter study examined the spatial distributions stratified by absorption, while here the stars are stratified by individual YSO evolutionary classification. The features of the spatial distribution visible in Figs. 6 and 7 include: the OMC-1S core, BN/KL core and northern extension which are part of the larger filament along the middle of the Orion A cloud and finally the East-West asymmetry that in Feigelson et al. (2005) was attributed to non-equilibrium dynamics. The latter only shows up in Class III systems.

The spatial distributions of Class II and III stars are also in agreement with the spatial distribution found by Hillenbrand (1997) who, using D'Antona & Mazzitelli (1994) isochrone ages, found that youngest stars are clustered toward the cluster center while slightly older stars are more widely distributed. The elongated asymmetric distribution of our candidate Class 0-I stars and the large-scale EW asymmetry are consistent with the distribution derived by Hillenbrand & Hartmann (1998) who concluded that the structure of the ONC is more the result of the different environmental conditions rather than the result of dynamical evolution.

There is a lower percentage of Class II objects in the central region, but this could be due to the reliance on the  $8.0\ \mu\text{m}$  detections for the selection of Class II stars. Our spatial distribution are, there-

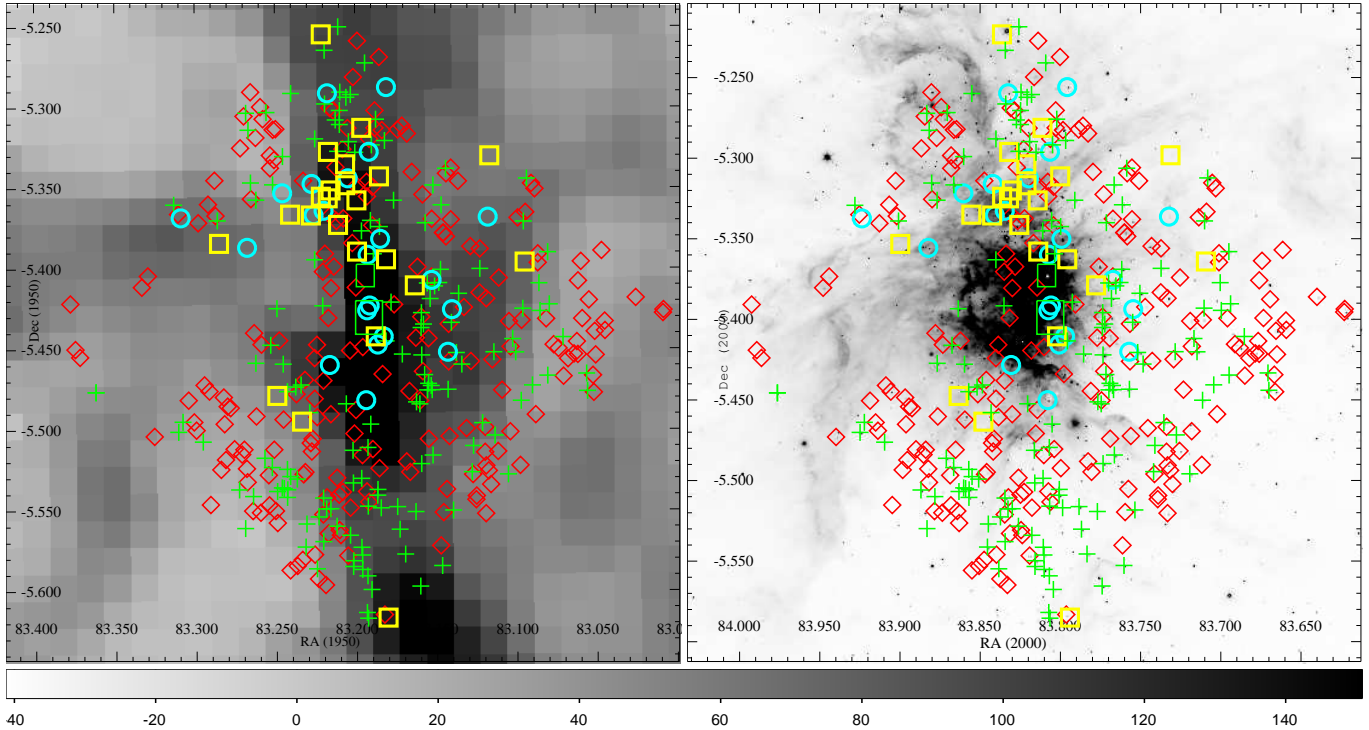


Fig. 7.— (Left) Velocity integrated  $^{13}\text{CO}$  emissivity from Bally et al. (1987) in the region around the Trapezium cluster and (right) *Spitzer* IRAC image at  $3.6\ \mu\text{m}$  in the same region. Both images are shown with inverted color map. Yellow squares and light blue circles indicate Class 0-Ia and 0-Ib objects, green plus symbols are Class II stars while red diamonds are Class III stars. The  $40'' \times 50''$  upper green box indicates the BN-KL region while the  $60'' \times 75''$  bottom green box indicates the Orion Molecular Cloud 1 South (OMC-1S).

fore, strongly dependent on the sensitivity of our NIR data which is quite limited toward the central region, where the contamination by the bright OB stars and nebular emission is very high.

## 5. EVOLUTION OF X-RAY ACTIVITY

The very deep X-ray COUP data together with the relatively large sample of Class 0-I objects selected with the *Spitzer* observations allow us, for the first time, to analyze and compare, in a statistically significant way, the X-ray properties of the YSOs in their initial protostellar phase with those of more evolved PMS stars.

As already mentioned in Section 3, we find that the fraction of Class 0-Ia objects detected in the X-rays is almost 40% (10/23), that of Class 0-Ib and Class III is about 80% (18/22 and 160/205, respectively) while that of Class II objects is about 88% (130/148). The analysis described in this section

aims at understanding whether the X-ray emission can be related to the IR properties of YSOs, which we take as signposts for the different phases of protostellar and PMS evolution.

### 5.1. X-ray luminosities

We use the results of the spectral analysis presented by Getman et al. (2005b) to compare the X-ray properties of the different populations of YSOs in the ONC. For the X-ray luminosities of detected stars we adopt the absorption corrected luminosities in the total 0.5–8.0 keV band,  $L_{t,c}$ , from Table 8 of Getman et al. (2005b).

In order to compare unbiased luminosity functions of the different classes, we derive upper limits to the X-ray luminosities of the X-ray undetected objects. Upper limits to the photon count rates of the 13+4 undetected Class 0-Ia and Class 0-Ib objects were calculated with PWDe-

tect (Damiani et al. 1997a,b) consistently with the source detection procedure of the other COUP sources (Getman et al. 2005b), adopting a detection threshold significance of  $5\sigma$ . The upper limits for the 9 undetected Class II stars and for the 2 undetected Class III stars were taken from Table 11 of Getman et al. (2005b).

In order to convert upper limits to the count rates into unabsorbed X-ray luminosities, we derive an extinction dependent conversion factor. The CCDs in Fig. 3 indicate that X-ray detected and undetected Class 0-I objects have similar reddening. We therefore computed the conversion factors of the X-ray detected Class 0-I objects as the ratio between the unabsorbed X-ray luminosities ( $L_{t,c}$ ) and the count rates taking into account the PSF fraction within the extracted area and the effective exposure time at the source position (Getman et al. 2005b), and we plotted these values as a function of the  $N_{\text{H}}^1$  values. We assume for the X-ray undetected Class 0-I objects a conversion factor computed as the median value of the conversion factors of the X-ray detected Class 0-I objects, which corresponds for these stars to  $N_{\text{H}} \simeq 4.5 \times 10^{22} \text{ cm}^{-2}$ . However, in order to check whether our results are robust with respect to the assumed  $N_{\text{H}}$  of undetected objects, we also considered the conversion factors corresponding to the highest and minimum conversion factors of the X-ray detected Class 0-I objects.<sup>2</sup> We used the same procedure to estimate the upper limits to the X-ray luminosities in the 2.0–8.0 keV hard band.

The X-ray properties of the Class 0-I COUP X-ray sources, taken from Getman et al. (2005b), are given in Table 9. We provide sequential numbers from our catalog, sequential COUP numbers, background-corrected counts in the 0.5–8.0 keV band, the fractions of the PSF within the source extraction areas, effective exposure times, the hydrogen column densities obtained from the spectral fit, plasma temperatures, emission measures and finally the absorption-corrected X-ray luminosities in the 2.0–8.0 keV hard band,  $L_{h,c}$ , and in the 0.5–8.0 keV total band,  $L_{t,c}$ .

<sup>1</sup>The H column densities were derived by Getman et al. (2005b) from the spectral analysis of the COUP sources.

<sup>2</sup>We used the median conversion factor to derive the X-ray luminosity ( $\log L_{t,c} = 28.52 \text{ erg/s}$ ) of the COUP source 1197 for which Getman et al. (2005b) did not perform a spectral fit because of the low counting statistics.

Values computed for the X-ray undetected Class 0-I stars are given in Table 10. We list sequential numbers from our catalog, the celestial coordinates from the *Spitzer* catalog, upper limits to the source counts computed with PWDetect in the hard and total bands, the effective *Chandra* exposure time at the object positions and, finally, the upper limits to the unabsorbed X-ray luminosities in the hard and total energy bands.

X-ray properties of X-ray detected Class II and III stars, taken from Getman et al. (2005b), are given in Tables 11 and 12 where column names are analogous to those given in Table 9.

The X-ray luminosities of X-ray undetected Class II and III objects were derived, as for Class 0-I stars, using the median conversion factor of the X-ray detected stars in the same class. This assumption is based on the fact that the NIR colors of the X-ray undetected Class II stars indicate that these objects are not more absorbed than those detected with COUP. In addition, the conversion factors corresponding to the lowest and highest observed  $N_{\text{H}}$  values were also considered ( $10^{21}$  and  $4.0 \times 10^{22} \text{ cm}^{-2}$  for the Class II stars and  $0.5 \times 10^{21}$  and  $2.0 \times 10^{22} \text{ cm}^{-2}$  for the Class III stars). Values computed for the X-ray undetected Class II and III stars are given in Table 13, analogous to Table 10.

## 5.2. X-ray luminosity functions

We now compare the X-ray luminosity functions of the stars of the four considered NIR classes. In order to take into account nondetections, XLFs were derived using the Kaplan-Meier maximum-likelihood estimator. For Class II and III sources, we considered separately stars in the three mass ranges used by Preibisch & Feigelson (2005). Fig. 8 shows the comparison of the XLFs of the four populations. The red and green lines indicate the XLF of Class III and II objects, respectively, with masses in the given range, while the black and blue lines are the XLFs of Class 0-Ia and 0-Ib stars, for which masses are unknown and are therefore the same in the three panels. Lines of the same color in each panel show the XLF obtained using the three different count rate to luminosity conversion factors adopted for the X-ray non detections of each subsample and give an idea of the uncertainty of the XLFs. We removed from this analysis the four objects of our sample of Class 0-Ia protostars without detections

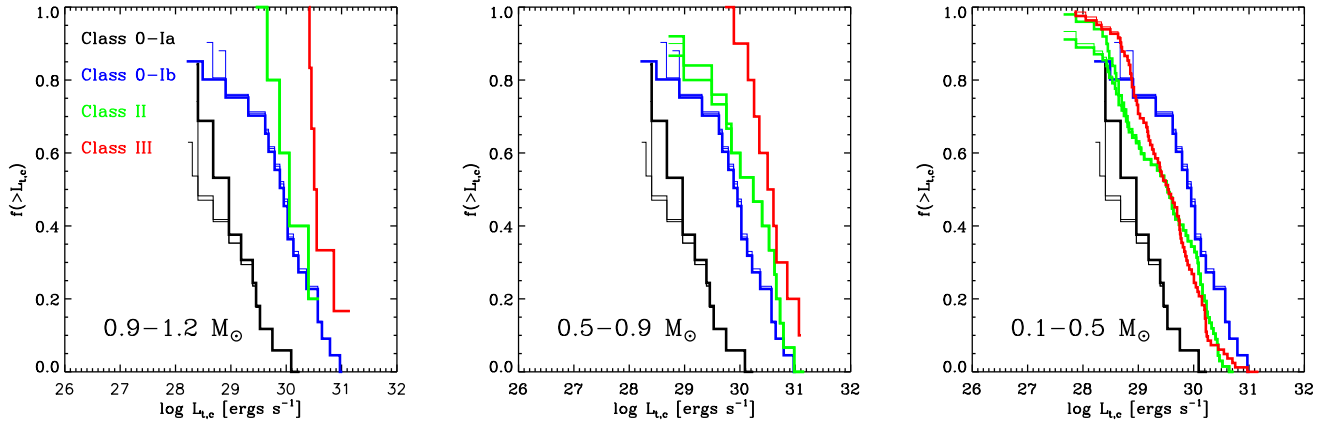


Fig. 8.— Maximum likelihood cumulative XLF in the total (0.2–8.0) keV energy band of the four NIR classes. The three panels refer to Class II and Class III stars in three different mass ranges. The red and green lines indicate the XLF of Class III and II objects, respectively, with masses in the given range, while the black lines are the XLF of Class 0-I stars, for which masses are unknown and are therefore the same in the three panels. Lines of the same color in each panel show the XLF computed using the three different luminosity conversion factors for the X-ray non detections. Thick lines indicate the XLF used to perform the statistical tests (see text). Note that the distributions do not reach the  $f=100\%$  because of the presence of upper limits.

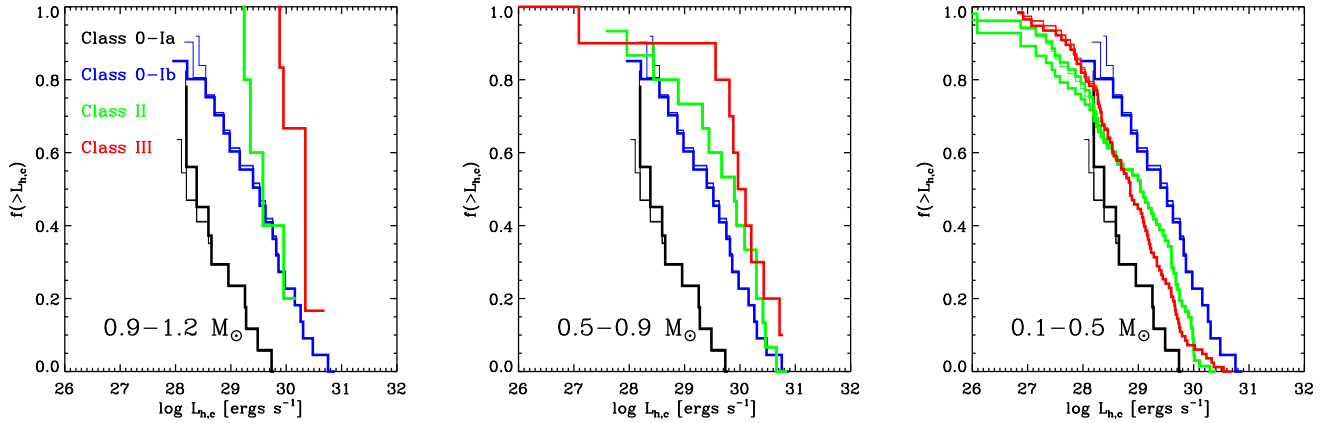


Fig. 9.— Maximum likelihood cumulative XLF in the hard (2.0–8.0) keV energy band of the four NIR classes. The figure is analogous to Fig. 8.

at  $4.5 \mu\text{m}$ . Since this band is one of the most sensitive bands and the least contaminated by nebulosity, these objects could be PAH contaminated sources or even knots of nebulosity. By discarding these objects, we are more confident to consider a sample of protostar candidates as less contaminated as possible. The figure shows that for the

two highest mass ranges, the X-ray luminosities of Class III stars are highly elevated with respect to those of Class II stars and 0-Ib objects. These latter two classes have very similar XLFs and are significantly brighter than Class 0-Ia stars.

Because the Class 0-Ia and Class 0-Ib stars in our sample are heavily absorbed, a note of

caution is needed. Since absorption precludes the observation of the soft part of the intrinsic source X-ray spectra, we cannot rule out the presence of soft, completely absorbed emission from Class 0-I stars. Nevertheless, we know from previous studies of CTTS stars that a very soft component,  $kT < 0.3$  keV, in the few cases in which it is observed, is mainly due to accretion (Kastner et al. 2002; Schmitt et al. 2005; Güdel et al. 2007; Argiroffi et al. 2007; Huenemoerder et al. 2007; Grosso et al. 2007), while harder components are due to coronal-like emission. This is in agreement with the previous finding for Class II stars in other regions (e.g. Stelzer & Schmitt 2004), where the X-ray spectra of Class II's were found to include an additional softer emission component compared to WTT's. Our Orion stars are too heavily absorbed to detect this soft component.

Coronal emission, as analyzed with resolution spectra from *Charge Coupled Devices*, can usually be decomposed into softer  $\sim 0.8$ – $1.0$  keV and harder  $\sim 2$  keV components (Preibisch et al. 2005). The soft coronal component, like the accretion component, might remain unobserved in heavily extincted sources such as our Class 0-I stars and thus the X-ray luminosities in the total band can underestimate the true emission in such objects. In addition, magnetic flare components can be strong around  $0.5$ – $2.0$  keV, and dominate the X-ray flux. For these reasons, we also considered the comparison of the XLFs of different classes, by restricting the analysis to the X-ray luminosities in the hard ( $2.0$ – $8.0$ ) keV energy band. We note that we recomputed with PWDetect the upper limits in the hard band for a total of 31 undetected objects, assuming a threshold of  $4.8\sigma$  estimated from the background in this band. Among these objects, 12 are flagged by the PWDetect code as affected by a X-ray detected source nearby, which therefore raises the upper limit count rate. In two cases out of 12, however, the asymmetry of the Chandra PSF at large off-axis angles is such as to make PWDetect clearly overestimate the contribution of the detected source to the computed upper limit at the desired position, which is instead dominated by the background; in these instances we computed the upper limit from the background alone. The results of this analysis are shown in Fig. 9, analogous to Fig. 8 but for the hard energy

band.

To check if these results are statistically significant, we performed statistical tests developed for “survival analysis”, suited for the analysis of censored datasets. The probabilities that the X-ray luminosities of the stars in two samples are drawn from the same parent distribution were computed with the ASURV<sup>3</sup> package (Feigelson & Nelson 1985). The results of this analysis are given in Tables 2 and 3 where, for each pair of samples, we list the probabilities computed using the five tests of the ASURV package. We note that the tests were performed in the most conservative way, i.e. by considering for each pair of samples the nearest XLFs among those computed with different conversion factors for the upper limits. The tests show that Class 0-Ia and 0-Ib stars have statistically different XLFs both in the hard and total bands, at a significance level larger than 99%; Class 0-Ia and II are different at a significance level of 99% for the  $[0.9$ – $1.2]$  and  $[0.5$ – $0.9]$   $M_{\odot}$  mass ranges. The difference is marginal, both in the total and hard band, for the  $[0.1$ – $0.5]$   $M_{\odot}$  mass range. The difference between Class II and III objects is quite marginal (between 85% and 95%) for the highest mass range, while for lower mass stars, Class II and III stars do not show any significant difference.

These results clearly indicate an evolution of the X-ray activity from Class 0-Ia, the least X-ray luminous objects, up to Class III, which show the highest X-ray luminosities, at least for stars with mass larger than  $0.9 M_{\odot}$ . Although the difference in the intrinsic X-ray activity between Class II and III stars is quite marginal, it is in agreement with previous results indicating that the X-ray luminosities of accretors in the ONC are smaller than those of non accretors (Flacomio et al. 2003b; Preibisch et al. 2005). Note, however, that these results cannot be compared directly because of the different criteria adopted to select the two populations.

The most significant and novel result is the difference in X-ray activity level between Class 0-Ia and Class II and between Class 0-Ia and Class 0-Ib sources. Our results are even more robust if we include the four objects without detections at  $4.5 \mu\text{m}$ .

<sup>3</sup>Astronomy Survival Analysis available from the StatCodes <http://www.astro.psu.edu/statcodes>

Table 2: Probabilities of correlation between the XLFs in the total band (0.2–8.0) keV of two samples, computed with the ASURV package (see Section 5.2).  $P_1$  and  $P_2$  are the probabilities computed using the Gehan generalized Wilcoxon test with permutation and hypergeometric variance, respectively,  $P_3$  is the probability from the Logrank test while  $P_4$  and  $P_5$  are the probabilities from the Peto and Peto and from the Peto and Prentice generalized Wilcoxon tests, respectively.

Mass [ $M_\odot$ ]	$P_1$ [%]	$P_2$ [%]	$P_3$ [%]	$P_4$ [%]	$P_5$ [%]	Sample 1	Sample 2
–	0.23	0.21	3.13	0.36	0.25	Class 0-Ia	Class 0-Ib
[ 0.9– 1.2 ]	0.35	0.07	0.03	0.46	0.45	Class 0-Ia	Class II
[ 0.9– 1.2 ]	94.75	94.99	62.55	97.88	97.73	Class 0-Ib	Class II
[ 0.9– 1.2 ]	6.79	5.10	16.15	16.15	–	Class II	Class III
[ 0.5– 0.9 ]	0.04	0.02	0.06	0.05	0.03	Class 0-Ia	Class II
[ 0.5– 0.9 ]	35.94	35.60	58.58	36.77	36.64	Class 0-Ib	Class II
[ 0.5– 0.9 ]	33.13	32.21	14.63	31.51	32.68	Class II	Class III
[ 0.1– 0.5 ]	5.28	5.64	23.77	6.04	5.53	Class 0-Ia	Class II
[ 0.1– 0.5 ]	3.41	2.02	1.52	3.43	2.88	Class 0-Ib	Class II
[ 0.1– 0.5 ]	86.08	86.09	40.72	80.37	80.34	Class II	Class III

Table 3: Probabilities of correlation between the XLFs in the hard band (2.0–8.0) keV of two samples, computed with the ASURV package (see Section 5.2). The probabilities are those described in Table 2.

Mass [ $M_\odot$ ]	$P_1$ [%]	$P_2$ [%]	$P_3$ [%]	$P_4$ [%]	$P_5$ [%]	Sample 1	Sample 2
–	0.36	0.36	2.99	0.53	0.47	Class 0-Ia	Class 0-Ib
[ 0.9– 1.2 ]	0.57	0.15	0.08	0.72	0.73	Class 0-Ia	Class II
[ 0.9– 1.2 ]	94.84	95.04	46.15	93.70	94.39	Class 0-Ib	Class II
[ 0.9– 1.2 ]	6.54	4.77	9.37	9.37	–	Class II	Class III
[ 0.5– 0.9 ]	0.08	0.05	0.89	0.12	0.08	Class 0-Ia	Class II
[ 0.5– 0.9 ]	28.18	27.57	56.83	29.37	28.97	Class 0-Ib	Class II
[ 0.5– 0.9 ]	62.80	62.59	34.13	61.58	62.47	Class II	Class III
[ 0.1– 0.5 ]	14.23	14.57	45.40	16.79	16.58	Class 0-Ia	Class II
[ 0.1– 0.5 ]	3.62	2.19	2.05	3.70	3.02	Class 0-Ib	Class II
[ 0.1– 0.5 ]	46.63	46.63	91.93	50.19	50.23	Class II	Class III

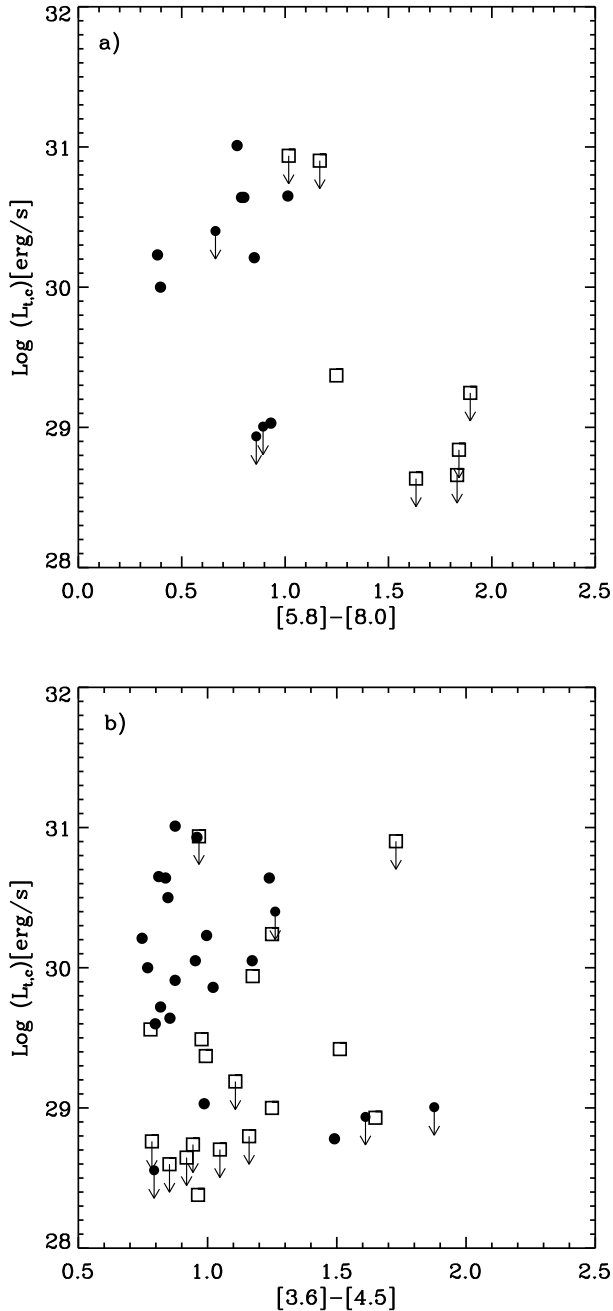


Fig. 10.— Absorption corrected X-ray luminosity of Class 0-Ia stars (squares) and Class 0-Ib (circles) as a function of the [5.8]-[8.0] (panel a) and [3.6]-[4.5] (panel b) colors. Upper limits are indicated by arrows.

Based on our selection criterion, Class 0-Ia objects are protostars with SEDs increasing up to  $8.0 \mu\text{m}$ , while Class 0-Ib are protostars with SEDs increasing up to  $4.5 \mu\text{m}$  and decreasing at longer wavelengths. Fig. 10a shows the absorption corrected X-ray luminosities plotted vs. the [5.8]-[8.0] color, that discriminates Class 0-Ia stars (squares) from Class 0-Ib ones (filled circles), the former being redder than  $[5.8]-[8.0] \simeq 1.1$  and the latter bluer than this value. This plot indicates a trend of increasing X-ray luminosity with decreasing [5.8]-[8.0] color. Fig. 10b shows the same luminosities as a function of the [3.6]-[4.5] color. While this latter color does not discriminate between Class 0-Ia and 0-Ib objects, it clearly confirms that, from the X-ray point of view, Class 0-Ia and 0-Ib objects belong to two different populations. This again suggests us that the contamination by reddened Class II objects can be very high for Class 0-Ib objects, while the Class 0-Ia sample is dominated by true protostars. We could then be witnessing the onset of X-ray activity in very young YSOs.

Class 0-I objects are affected by larger absorptions with respect to the other classes as we will confirm in Sect. 5.3 using the X-ray derived  $N_{\text{H}}$  values. Can this fact result in a systematic underestimation of  $L_{\text{X}}$  values for Class 0-I stars? Although we do apply absorption corrections to the observed X-ray fluxes when deriving luminosities both in the 0.5-8.0 keV and 2.0-8.0 keV bands, these are corrections to the *observed* X-ray spectra and emission from relatively cool plasma would remain unobserved, and therefore unaccounted for, in heavily absorbed sources.

In order to verify that the X-ray luminosities of heavily absorbed Class 0-I objects are accurately corrected for absorption, we assumed that these sources have X-ray spectra similar to Class II and III objects, and computed through extensive simulations the effect of varying the absorbing hydrogen column density on the determination of X-ray luminosities.

For this purpose we considered the best fit spectra of a subsample of  $\sim 200$  Class II and III objects with small absorption ( $\text{Log } N_{\text{H}} < 21.5 \text{ cm}^{-2}$ ), consisting of either one or two thermal components. For each of these spectra, using XPSEC and the FAKEIT command, we computed 10 simulated spectra for each of five different  $N_{\text{H}}$  values in the range  $10^{21} \text{ cm}^{-2} < N_{\text{H}} < 10^{23} \text{ cm}^{-2}$ . We then

analyzed the simulated spectra with a procedure analogous to that used by Getman et al. (2005b) for the analysis of the observed spectra. Each spectrum was rebinned so to have a minimum of 15 photon per channel and was then fit with both an isothermal and a two component model. After adopting the simplest of the two models that gave a statistically acceptable fit, we computed the unabsorbed flux in the 0.5-8.0 keV and 2.0-8.0 keV bands. We then computed the absorption corrected XLFs for each of the five absorption values. Most of the simulated sources did not have enough photons when absorbed by  $N_H = 10^{23} \text{cm}^{-2}$ . In order to avoid selection effects, since we are not accounting for upper limits, we could only compare the XLFs for the 115 sources whose spectra were bright enough to be analyzed even when considering the highest absorption value. The result is that the 5 XLFs for the 0.5-8.0 keV luminosities have median within  $\sim 0.1$  dex but tend to become wider as the  $N_H$  is increased. The five XLFs for 2.0-8.0 keV luminosities are instead very similar in shape and with medians within 0.03 dex, except for the one relative to the highest absorption values which is *brighter* by  $\sim 0.1$  dex. We conclude that, in the assumption that Class 0-I sources have the same spectra of Class II-III ones, the X-ray luminosities we derive are not underestimated.

We cannot exclude that some of the Class 0-Ib stars are actually heavily absorbed Class II stars (see Fig. 3). However, even in this case, our result would plausibly indicate a significant evolution of X-ray activity in the early stages of YSO formation.

Due to various IR sensitivity limitations at very high obscurations, the Class 0-I sampling might be restricted to higher masses (with stronger IR bolometric luminosities), and through the  $L_X$ -mass correlation, would have higher  $L_X$  values introducing a bias. But we find that these heavily obscured stars have lower, not higher,  $L_X$  values, further supporting our result.

Another bias may be introduced by the requirement that all stars considered have IRAC detections in one or more bands. Therefore, it is possible that lower-mass (i.e. bolometrically weaker) Class III stars have been systematically omitted from the sample, leaving behind too many higher mass, i.e. stronger  $L_X$  stars. But this is not relevant as the XLF comparisons in Figs. 8 and 9 are

binned by mass. We might have few 0.1–0.5  $M_\odot$  Class III stars, but those shown should be unbiased in  $L_X$ .

Another possible worry is that flares could dominate the flux from some of our objects, and our X-ray spectra could pertain to the flaring state rather than the quiescent state. We have verified that this is not the case by using the technique described in Wolk et al. (2005) to recompute X-ray spectra and fluxes for our stars using photons detected only during non-flaring intervals. Fits to these new spectra yield XLFs that do not differ significantly from those shown in Fig. 8. We have also verified that using these new spectra the results discussed in the next section do not change significantly.

We note that our results are consistent with the non-detection of class 0 sources of Serpens (Giardino et al. 2007). In fact, their limiting sensitivity, ( $4.0 \times 10^{29}$  erg/s in the hard band) estimated assuming temperature and absorption similar to those we found for our X-ray detected Class 0-I sources, corresponds to the highest tenth percentile of the XLF of our Class 0-Ia stars. Considering the small size of the Serpens Class 0 star sample, their non-detection is not surprising.

### 5.3. Gas and dust absorption

Figure 11 shows the *Spitzer*/IRAC [3.6]-[4.5] color vs. *Chandra* X-ray median energy of all selected sources. The typical uncertainty in the median energy has been estimated using the results of the MARX simulations made in Getman et al. (2006), where the median energy errors were computed as a function of the source net counts. We used the value of 0.3 keV, corresponding to objects with  $\text{MedE} \gtrsim 2$  keV and with about 30 net counts which is the minimum of net counts we have for Class 0-I objects. The typical uncertainty in the IRAC color has been estimated assuming a 5% uncertainty for the IRAC magnitudes.

As discussed in Getman et al. (2007), high X-ray median energy ( $\text{MedE} \gtrsim 1.7$  keV) can be considered as an indicator of absorbing column density that arises from gas, primarily metallic elements (e.g. N, O, Ne, Mg, Si, Ar, Fe, etc.). On the other hand, if the object is known to be a protostar, the [3.6]-[4.5] color is primarily a measure of the density of grains in the local infalling

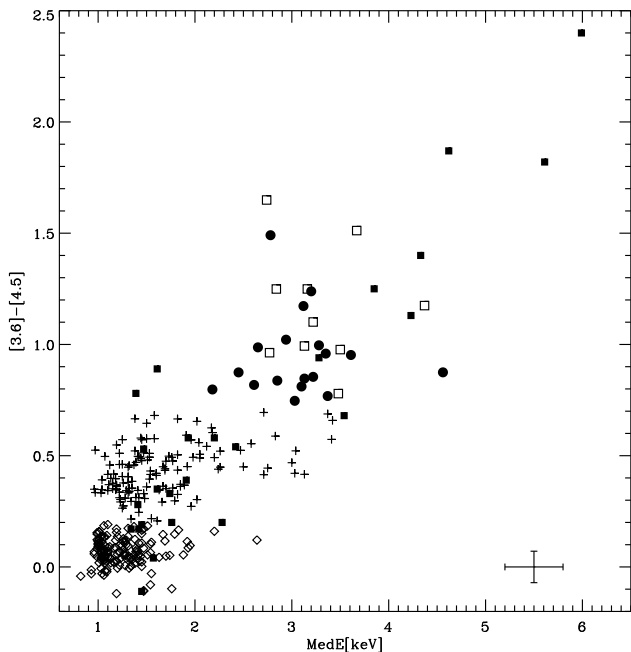


Fig. 11.— *Spitzer*/IRAC [3.6]-[4.5] color vs. *Chandra* X-ray median energy of all selected sources. The different classes ONC objects are indicated using the same symbols of Fig. 5, while filled squares are the values of the YSO in IC 1396N taken from Getman et al. (2007). Typical error bars in the median energy and in the IRAC colors are also shown.

envelope. Thus, the correlation between these two quantities, first found in Getman et al. (2007), has been interpreted by these authors as evidence of absorption from the protostellar envelope rather than from the ambient molecular cloud material. Although our data do not cover the whole X-ray median energy, they show a trend consistent with that found using the IC 1396N data, also shown in Fig. 11. Nevertheless, the interpretation of our data is not as clear as it was in IC1396N, since the ONC background is quite complex while the maximum line-of-sight column is  $A_V \sim 10$  mag.

Fig. 12 compares the absorbing column density  $N_H$  for the different populations. In the left panel,  $\log N_H$  is plotted for the X-ray detected objects as a function of the unabsorbed X-ray luminosity  $L_{t,c}$ . The right panel shows, for each class, the median values of the absorbing column density distri-

butions, values between the first and third quartiles and values between the minimum and the maximum of the distributions of the  $\log N_H$  values. Note that only objects with errors in  $\log N_H$  smaller than 0.5 have been considered. However, the median values of the distribution do not change significantly if all data are considered.

A clear trend of increasing absorbing column density from Class III to Class 0-I can be seen both in the left and right panels. This trend is expected since Class 0-I objects are characterized by a large amount of infalling material and are also typically embedded in the molecular cloud; a smaller amount of obscuring material is instead present for Class II objects that have shed their envelope and formed a circumstellar disk, while the extinction suffered from Class III objects is due to interstellar material only (both within the cloud and on the line of sight to the cloud).

We note that the estimate of the  $N_H$  values of Class 0-I stars is based primarily on the hard component of the X-ray spectrum. That is, at the temperatures of the protostars ( $kT_{av} \sim 2$  keV) and with  $\log N_H \sim 23 \text{ cm}^{-2}$ , the observed flux is almost entirely due to the hard component of the X-ray spectrum. At the same temperatures, if the  $N_H$  was smaller, the total flux would be distributed between the soft and hard component and the shape of the spectrum would be different. Our technique should thus be the most accurate for objects with high  $N_H$  values – thus yielding particularly good  $N_H$  values for the, on average, heavily embedded protostars. Therefore, we argue that the low XLFs for protostars we have derived (see Figure 9) are unlikely to be due to errors in our estimates of the X-ray absorption towards these objects, as confirmed from the analysis of the hard XLFs and the simulated spectra of Class II and III (see Sect. 5.2).

#### 5.4. Evolution of YSO X-ray spectra and temporal characteristics

Fig. 13 shows the results of the comparison of the average plasma temperature  $kT_{av}$  amongst the different classes. For X-ray spectra fit with two isothermal components,  $kT_{av}$  was computed as the mean of the soft and hard  $kT$  spectral components, weighted by their respective emission measures; for spectra fit with a single component  $kT_{av} = kT$ . The  $kT_{av}$  values for the X-ray detected objects

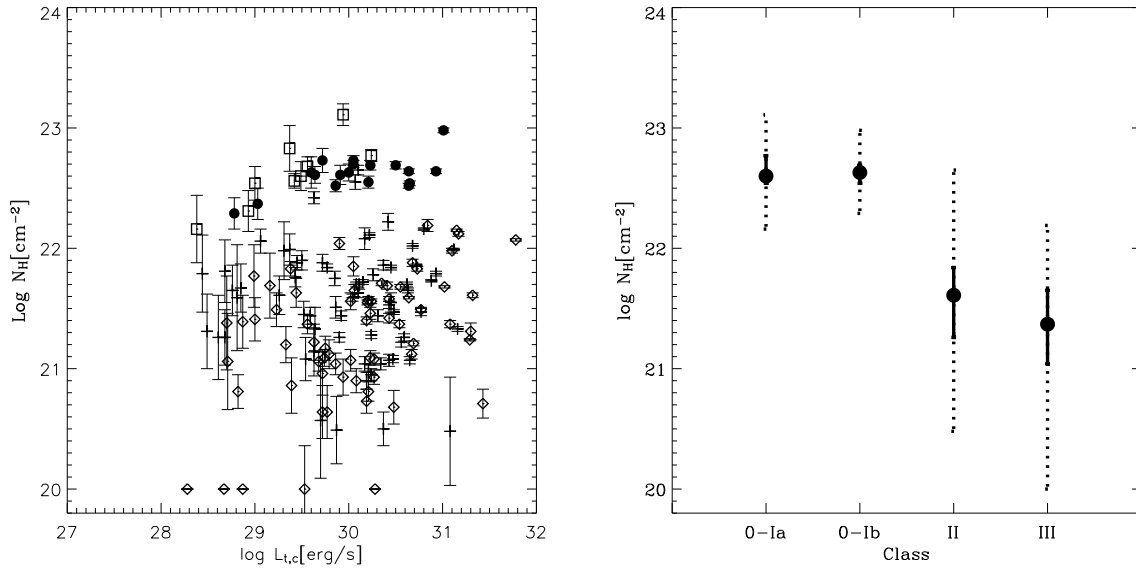


Fig. 12.— Left panel shows the  $\log N_{\text{H}}$  values as a function of the unabsorbed X-ray luminosity  $L_{t,c}$  for the X-ray detected objects. Symbols are as in Fig. 5. Right panel shows, for each class, the median values of the absorbing column density distributions indicated by the big black dots. Solid bars indicate the values of  $\log N_{\text{H}}$  included between the first and third quartiles, while the dashed lines (partially hidden by solid bars) indicate the values included between the minimum and the maximum of the distributions of the  $\log N_{\text{H}}$  values. Note that only objects with errors in  $\log N_{\text{H}}$  smaller than 0.5 were considered.

of the different populations are plotted as a function of the unabsorbed X-ray luminosity  $L_{t,c}$ . Note that only objects with errors on  $kT_{av}$  smaller than 1 keV have been considered. However the distributions do not change significantly if all data are considered. The bottom-right panel of Fig. 13 shows, for each class, the median values of the average plasma temperatures, values between the first and third quartiles and values between the minimum and the maximum of the distributions of the  $kT_{av}$  values. No trend in plasma energy is found as a function of evolutionary stage from Class 0-Ia to Class III systems.

A trend of increasing of the average plasma temperature with increasing unabsorbed X-ray luminosity is clearly evident for all the samples, as has often been reported for other types of coronal sources (e.g. Schmitt et al. 1990). A similar result is obtained by considering only the sub-sample of stars with X-ray spectra fit with two temperature components: high luminosity stars tend to have high values of the ratio between the high and low temperature emission measures ( $EM_2/EM_1 \sim 2.5$ ), suggesting that the hot plasma component dominates over the cold one for the high luminosity stars. No significant difference between the classes is observed in Fig. 13.

Finally we checked if ONC stars of different classes show different X-ray temporal behavior. To do this, we used the results of the nonparametric one-sample Kolmogorov-Smirnov (K-S) test performed by Getman et al. (2005b). The results of the K-S test,  $P_{KS}$ , strongly depend on the source count-statistics and therefore on their count rate. For this reason, we compared the probabilities of variability  $P_{var}=(1-P_{KS})$  for the different classes of stars with count rates in definite ranges. The results are given in Table 4 where, for each class and for a given range of Count Rate (CR), we report the number of stars with  $P_{var} > 99\%$  with respect to the total number of stars of each class in the corresponding range of count rates. The percentage of variable stars is also indicated within brackets. Even if the statistics for each sample is quite poor, the percentages indicate that the different classes have very similar fractions of variable stars. In practice, when observed with high statistics, all the sources are variable, independently on their class.

## 6. CLASS 0-I: COUNTERPARTS AT OTHER WAVELENGTHS

We list in Table 14 the counterparts of the Class 0-I objects identified in this work that have been detected in X-rays (the COUP survey), JHKL bands (Lada et al. 2000; Muench et al. 2002, hereafter LMH00 and MLL02, respectively), 10 and 20  $\mu\text{m}$  (Robberto et al. 2005a, hereafter RBP5) and in the 11.7  $\mu\text{m}$  (Smith et al. 2005, hereafter SBS05). None of our candidate Class 0-I sources are in the list of 1.3 cm radio sources of Zapata et al. (2004b).

The JHKL photometric survey from Lada et al. (2000) included 391 stars in the central  $6'55 \times 6'55$  of the Trapezium cluster. By selecting stars with  $K - L > 1.5$ , they obtained a list of 78 candidate protostars. We correlated this list with our catalog using a matching radius of  $1''.2$ . As expected, the Lada et al. (2000) sample, selected on the basis of the  $K - L$  color, is larger than our sample for which the selection requires at least two colors computed using the K and the four IRAC magnitudes. For this reason, we find that only 4 of the 78 Lada et al. (2000) candidate protostars are in common with our Class 0-Ia stars and 9 with our Class 0-Ib stars. Among the remaining 65 objects, 16 cannot be Class 0-I objects since they have an optical counterpart in our catalog and 27 have  $[3.6]-[4.5] < 0.7$  and are therefore consistent with star-disk systems (Class II) rather than protostars; for the remaining 22 Lada et al. (2000) candidate protostars, the available magnitudes do not satisfy our selection criteria.

Among our Class 0-I objects, only 5 (Class 0-Ib) have been detected at 10 and 20  $\mu\text{m}$  by Robberto et al. (2005a); of these 5, 2 are in the list of the embedded objects previously studied in Smith et al. (2004, hereafter SBS04) in the OMC-1S region at 8.8, 11.7 and 18.8  $\mu\text{m}$ .

We interpolated the flux conversion coefficients given in Lada et al. (2006) to 10 and 20  $\mu\text{m}$  and we computed the corresponding fluxes. SEDs with all the available fluxes for these 5 objects are shown in Fig. 14.

In order to understand the properties of our sample of Class 0-I objects, we also considered the compact radio sources detected by Zapata et al. (2004b) and Zapata et al. (2004a) using, respectively, 1.3 cm (in a region of  $30'' \times 30''$  around

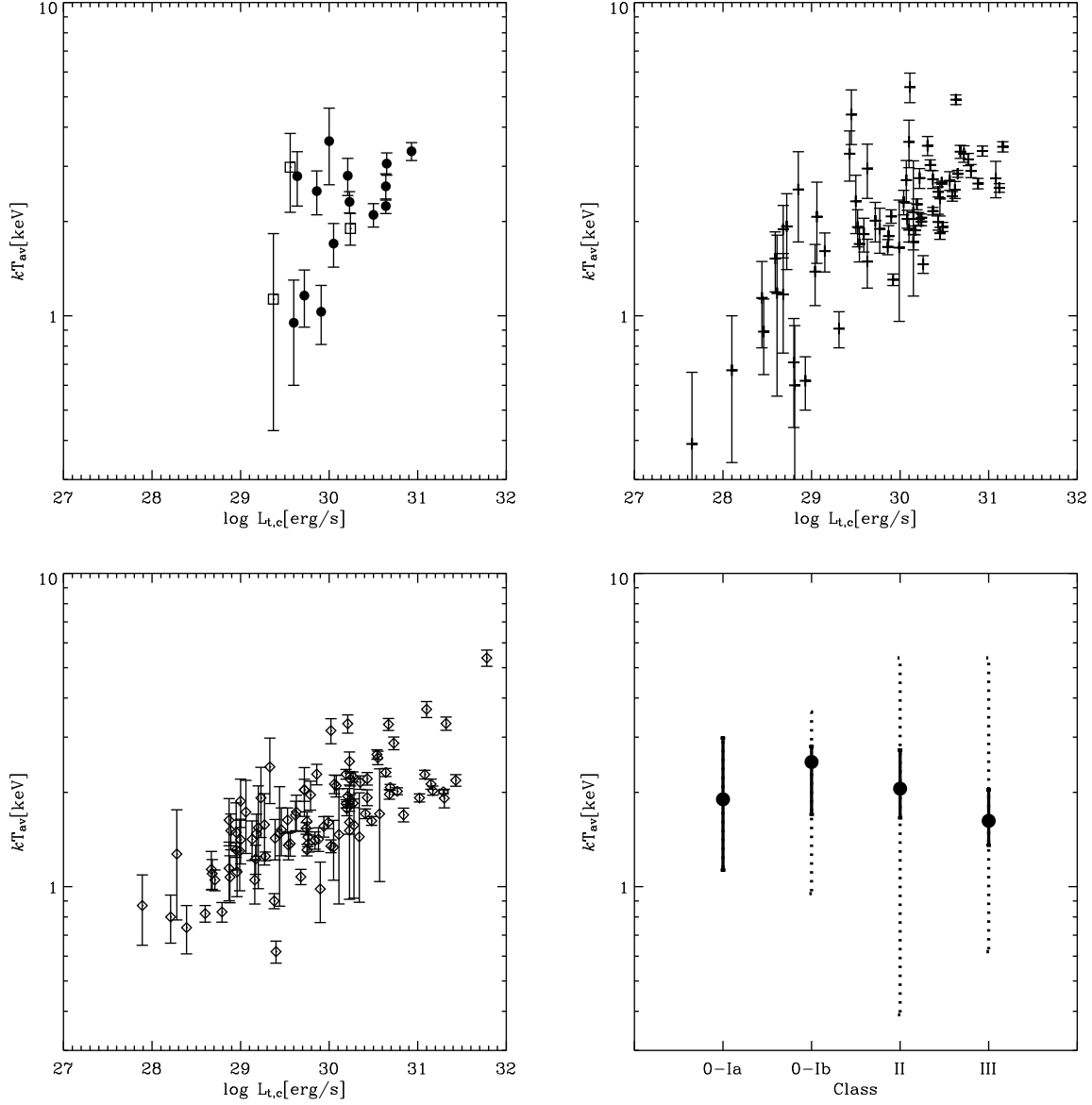


Fig. 13.—  $kT_{\text{av}}$  values as a function of the unabsorbed X-ray luminosity  $L_{t,c}$  for the X-ray detected objects, plotted separately for Class 0-I, Class II and Class III stars, in the first three panels. Symbols are as in Fig. 5. The bottom-right panel shows, for each class, the median values of the average plasma temperature distributions indicated by the big black dots. Solid bars indicate values of the temperature distributions between the first and third quartiles, while dashed lines (partially hidden by solid bars) indicate values between the minimum and the maximum of the distributions of the  $kT_{\text{av}}$  values. Note that only objects with errors in  $kT_{\text{av}}$  smaller than 1 keV were considered.

Table 4: X-ray variable sources of different evolutionary class stars in the ONC with  $P_{KS} > 99\%$ .

$\log(\text{CR})$	Class 0/Ia	Class 0/Ib	Class II	Class III
$[-5, -4]$	2/ 4 ( 50%)	0/ 2 ( 0%)	1/ 4 ( 25%)	0/ 2 ( 0%)
$[-4, -3]$	5/ 6 ( 83%)	6/ 9 ( 66%)	15/28 ( 53%)	19/30 ( 63%)
$[-3, -2]$	–	7/ 7 (100%)	38/38 (100%)	46/50 ( 92%)

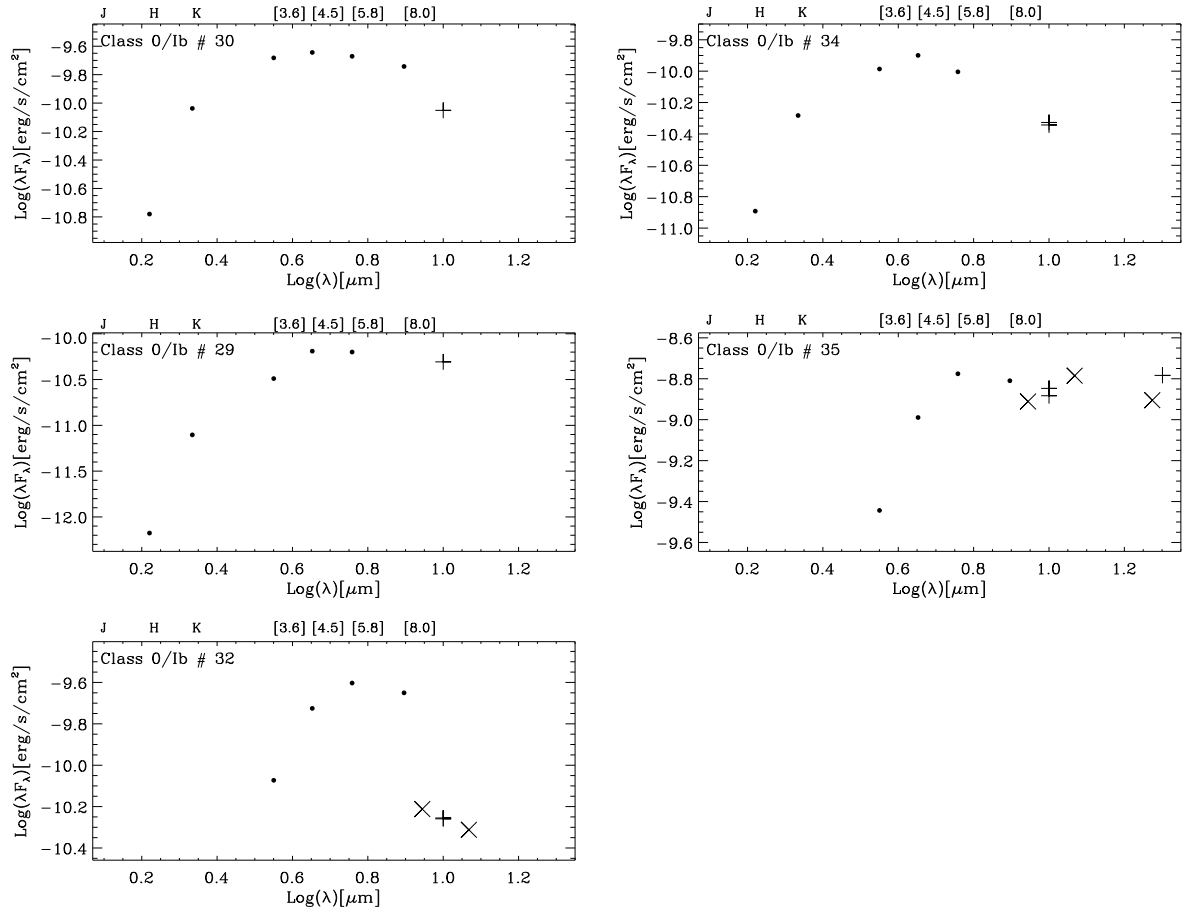


Fig. 14.— SED of Class 0-I candidate objects in the Robberto et al. (2005a) list with photometry at 10 and/or 20 μm. Dots indicate fluxes computed using the magnitudes from our catalog, plus symbols correspond to the magnitudes at 10 and 20 μm from the Robberto et al. (2005a) catalog and X correspond to the magnitudes at 8.8, 11.7 and 18.8 μm from the Smith et al. (2004) catalog. Multiple values at 10 μm are relative to the two different nights of observation in Robberto et al. (2005a).

OMC-1S) and 3.6 cm observations (in a region of  $4' \times 4'$  around the Trapezium cluster) performed with the Very Large Array. With a matching radius of  $1''$ , we retrieved in our catalog 7 of the 11 radio sources at 1.3 cm and 67 of the 77 compact 3.6 cm sources.

None of the Zapata et al. (2004a,b) matched sources is in our list of Class 0-I objects. The absence of 1 cm radio counterparts in our protostar sample might imply that the radio sources are mainly magnetically active non-thermal Class III stars rather than thermal protostellar outflows.

Note that the north-east region of the COUP FOV, where most of our candidate Class 0-I are concentrated, is not included in the FOV of the literature sources mentioned in this section. For this reason, the SEDs of Class 0-I objects in this region cannot yet be extended to wavelengths longer than  $8 \mu\text{m}$ , which is crucial to confirm (or refute) their protostellar nature.

Finally, our list of candidate Class 0-I protostars includes only two objects (COUP sources 420 and 484) of the list of stars studied in Grosso et al. (2005), located at the bottom edge of the OMC-1S region, i.e., far from the density peak and its associated nebular emission. We know that the absence of IRAC protostars near OMC-1s and in the BN/KL region is due to nebular contamination and crowding, not to the real absence of protostars in these two high density regions. In addition, we cannot classify the COUP sources 582, 594, 615, 633, 641, 659 and 667, indicated in Grosso et al. (2005) as embedded YSOs in a subcluster, since they do not have any counterpart at the IRAC bands.

## 7. SUMMARY AND CONCLUSIONS

We have selected a sample of 45 candidate Class 0-I objects in the ONC field observed in the X-rays by COUP using new deep *JHK*, [3.6], [4.5], [5.8] and [8.0] photometry obtained at the ISPI@4m CTIO telescope and from *Spitzer* IRAC observations. New deep optical observations taken with the WFPC2 camera of HST and the WFI camera of ESO 2.2 m were also used to reject candidate Class 0-I objects with optical counterparts.

We distinguish between candidate protostars with SEDs increasing monotonically from K up to  $8 \mu\text{m}$ , indicated as Class 0-Ia, and candidate pro-

tostars with SED increasing from K up to  $4.5 \mu\text{m}$  and decreasing at longer wavelengths, indicated as Class 0-Ib, since the different slope of the SED at wavelengths larger than  $4.5 \mu\text{m}$  could be an indicator of a different density in the circumstellar material.

Out of the 23 Class 0-Ia stars, 10 have been detected in the X-rays with COUP, while out the 22 Class 0-Ib stars, 18 have been detected; we are thus in the position to study, for the first time, the X-ray properties of a significant and homogeneous sample of candidate protostars.

Samples of bona fide more evolved Class II and III stars in the same region have also been selected in order to study the time and mass evolution of X-ray activity.

Our principal result is that Class 0-Ia stars are significantly less luminous in X-rays, both in the total and hard bands, than more evolved Class II stars with mass larger than  $0.5 M_{\odot}$ , while Class 0-Ib stars show X-ray luminosities similar to Class II stars; finally, our data confirm previous determinations (Neuhauser 1997; Flaccomio et al. 2003b; Preibisch et al. 2005) that Class III stars with masses  $>0.3 M_{\odot}$  are more X-ray luminous than Class II objects, even if the result is quite marginal with our data.

Our result that Class 0-Ia objects are less luminous in X-rays than objects of other classes, support the hypothesis that the onset of X-ray emission occurs at a very early stage, when the objects show an increasing SED at least up to  $8.0 \mu\text{m}$ . The lack of a detailed theory of protostellar evolution does not allow us to interpret the difference in the evolutionary stage between Class 0-Ia and 0-Ib protostars. Although Class 0-Ib objects are selected as candidate protostars, our data suggest that this sample could be dominated by reddened Class II stars. If we consider the X-ray limiting sensitivity in Giardino et al. (2007), we deduce that our results are in agreement with the non-detection of Class 0 protostars in Serpens.

The X-ray spectral properties of Class 0-Ia and 0-Ib are similar to those of the more evolved Class II and III objects except for a larger absorption likely due to the enhanced local density surrounding protostellar objects. The different evolutionary classes also show similar X-ray variability characteristics and the protostellar variability

ity is indistinguishable from T Tauri variability. This result supports the XEST determination that variability of Class II and III stars are the same (Stelzer et al. 2007) and the COUP determination that T Tauri M stars have the same variability as more massive stars (Caramazza et al. 2007). Also related is the COUP result that YSOs with high X-ray luminosities have the same first ionization potential-related elemental abundances as older flaring stars (Maggio et al. 2007).

All of these results support the general theme that there is only one mechanism in YSO X-ray production at energies  $\gtrsim 1$  keV, and that this mechanism arises from stellar magnetic activity which does not depend on accretion or disks. The various recent arguments (Kastner et al. 2002; Schmitt et al. 2005; Güdel et al. 2007; Argiroffi et al. 2007; Huenemoerder et al. 2007; Grosso et al. 2007) that accretion accounts for some X-ray emission and line ratios, probably only refers to soft components which are not accessible to our study (Feigelson et al. 2007).

This work is based on observations made with *Hubble* Space Telescope and the *Spitzer* Space Telescope, which is operated by the Jet Propulsion Laboratory (JPL), California Institute of Technology under a contract with NASA. Partial support for this work was provided by NASA through an award issued by JPL/Caltech, by ASI and INAF. EDF is supported by NASA contract NAS8-38252. This research has made use of NASA's Astrophysics Data System (ADS) Abstract Service, and of the SIMBAD database, operated at CDS, Strasbourg, France. This research has also made use of data products from the Two Micron All-Sky Survey (2MASS), which is a joint project of the University of Massachusetts and the Infrared Processing and Analysis Center, funded by the National Aeronautics and Space Administration and the National Science Foundation. These data were served by the NASA/IPAC Infrared Science Archive, which is operated by the Jet Propulsion Laboratory, California Institute of Technology, under contract with the National Aeronautics and Space Administration. We wish to thank Francesco Damiani and Konstantin Getman for helpful discussions. We also thank the anonymous referee for suggestions that helped improve this paper.

## REFERENCES

- Adams, F. C., Lada, C. J., & Shu, F. H. 1987, *ApJ*, 312, 788
- Allen, L., Megeath, S. T., Gutermuth, R., et al. 2007, in *Protostars and Planets V*, ed. B. Reipurth, D. Jewitt, & K. Keil, 361–376
- Allen, L. E., Calvet, N., D'Alessio, P., et al. 2004, *ApJS*, 154, 363
- Andre, P., Ward-Thompson, D., & Barsony, M. 1993, *ApJ*, 406, 122
- Argiroffi, C., Maggio, A., & Peres, G. 2007, *A&A*, 465, L5
- Bally, J., Stark, A. A., Wilson, R. W., & Langer, W. D. 1987, *ApJ*, 312, L45
- Caramazza, M., Flaccomio, E., Micela, G., et al. 2007, *A&A*, 471, 645
- Cutri, R. M., Skrutskie, M. F., van Dyk, S., et al. 2003, 2MASS All Sky Catalog of point sources. (The IRSA 2MASS All-Sky Point Source Catalog, NASA/IPAC Infrared Science Archive. <http://irsa.ipac.caltech.edu/applications/Gator/>)
- Damiani, F., Maggio, A., Micela, G., & Sciortino, S. 1997a, *ApJ*, 483, 350
- Damiani, F., Maggio, A., Micela, G., & Sciortino, S. 1997b, *ApJ*, 483, 370
- D'Antona, F. & Mazzitelli, I. 1994, *ApJS*, 90, 467
- Favata, F. & Micela, G. 2003, *Space Science Reviews*, 108, 577
- Fazio, G. G., Hora, J. L., Allen, L. E., et al. 2004, *ApJS*, 154, 10
- Feigelson, E., Townsley, L., Güdel, M., & Stassun, K. 2007, in *Protostars and Planets V*, ed. B. Reipurth, D. Jewitt, & K. Keil, 313–328
- Feigelson, E. D., Getman, K., Townsley, L., et al. 2005, *ApJS*, 160, 379
- Feigelson, E. D. & Nelson, P. I. 1985, *ApJ*, 293, 192
- Flaccomio, E., Damiani, F., Micela, G., et al. 2003a, *ApJ*, 582, 382

- Flaccomio, E., Damiani, F., Micela, G., et al. 2003b, *ApJ*, 582, 398
- Flaccomio, E., Micela, G., & Sciortino, S. 2003c, *A&A*, 397, 611
- Flaherty, K. M., Pipher, J. L., Megeath, S. T., et al. 2007, *ArXiv Astrophysics e-prints*
- Getman, K. V., Feigelson, E. D., Garmire, G., Broos, P., & Wang, J. 2007, *ApJ*, 654, 316
- Getman, K. V., Feigelson, E. D., Grosso, N., et al. 2005a, *ApJS*, 160, 353
- Getman, K. V., Feigelson, E. D., Townsley, L., et al. 2006, *ApJS*, 163, 306
- Getman, K. V., Flaccomio, E., Broos, P. S., et al. 2005b, *ApJS*, 160, 319
- Giardino, G., Favata, F., Micela, G., Sciortino, S., & Winston, E. 2007, *A&A*, 463, 275
- Grosso, N., Bouvier, J., Montmerle, T., et al. 2007, *A&A*, *ArXiv:astro-ph/0709.0404*
- Grosso, N., Feigelson, E. D., Getman, K. V., et al. 2005, *ApJS*, 160, 530
- Güdel, M., Skinner, S. L., Mel'Nikov, S. Y., et al. 2007, *A&A*, 468, 529
- Gutermuth, R. A., Myers, P. C., Megeath, S. T., et al. 2007, *ApJ*, *arXiv:astro-ph/0710.1860*
- Hamaguchi, K., Corcoran, M. F., Petre, R., et al. 2005, *ApJ*, 623, 291
- Hartmann, L., Megeath, S. T., Allen, L., et al. 2005, *ApJ*, 629, 881
- Herbst, W., Bailer-Jones, C. A. L., Mundt, R., Meisenheimer, K., & Wackermann, R. 2002, *A&A*, 396, 513
- Hillenbrand, L. A. 1997, *AJ*, 113, 1733
- Hillenbrand, L. A., Bauermeister, A., & White, R. J. 2007, *ArXiv:astro-ph/0703642*
- Hillenbrand, L. A. & Hartmann, L. W. 1998, *ApJ*, 492, 540
- Huenemoerder, D. P., Kastner, J. H., Testa, P., Schulz, N. S., & Weintraub, D. A. 2007, *ArXiv e-prints*, 708
- Kastner, J. H., Franz, G., Grosso, N., et al. 2005, *ApJS*, 160, 511
- Kastner, J. H., Huenemoerder, D. P., Schulz, N. S., Canizares, C. R., & Weintraub, D. A. 2002, *ApJ*, 567, 434
- Kenyon, S. J., Calvet, N., & Hartmann, L. 1993, *ApJ*, 414, 676
- Lada, C. J. 1987, in *IAU Symposium*, Vol. 115, *Star Forming Regions*, ed. M. Peimbert & J. Jugaku, 1–17
- Lada, C. J., Muench, A. A., Haisch, Jr., K. E., et al. 2000, *AJ*, 120, 3162
- Lada, C. J., Muench, A. A., Lada, E. A., & Alves, J. F. 2004, *AJ*, 128, 1254
- Lada, C. J., Muench, A. A., Luhman, K. L., et al. 2006, *AJ*, 131, 1574
- Lada, C. J. & Wilking, B. A. 1984, *ApJ*, 287, 610
- Maggio, A., Flaccomio, E., Favata, F., et al. 2007, *ApJ*, 660, 1462
- Megeath, S. T., Allen, L. E., Gutermuth, R. A., et al. 2004, *ApJS*, 154, 367
- Megeath, S. T., Flaherty, K. M., Hora, J., et al. 2005, in *IAU Symposium*, Vol. 227, *Massive Star Birth: A Crossroads of Astrophysics*, ed. R. Cesaroni, M. Felli, E. Churchwell, & M. Walmsley, 383–388
- Muench, A. A., Lada, E. A., Lada, C. J., & Alves, J. 2002, *ApJ*, 573, 366
- Neuhauser, R. 1997, *Science*, 276, 1363
- Ozawa, H., Grosso, N., & Montmerle, T. 2005, *A&A*, 429, 963
- Preibisch, T. & Feigelson, E. D. 2005, *ApJS*, 160, 390
- Preibisch, T., Kim, Y.-C., Favata, F., et al. 2005, *ApJS*, 160, 401
- Reach, W. T., Megeath, S. T., Cohen, M., et al. 2005, *PASP*, 117, 978
- Rebull, L. M., Hillenbrand, L. A., Strom, S. E., et al. 2000, *AJ*, 119, 3026

- Robberto, M., Beckwith, S. V. W., & Panagia, N. 2002, *ApJ*, 578, 897
- Robberto, M., Beckwith, S. V. W., Panagia, N., et al. 2005a, *AJ*, 129, 1534
- Robberto, M., O'Dell, R. C., Hillenbrand, L. A., et al. 2005b, in *Bulletin of the American Astronomical Society*, Vol. 37, *Bulletin of the American Astronomical Society*, 1404
- Schmitt, J. H. M. M., Collura, A., Sciortino, S., et al. 1990, *ApJ*, 365, 704
- Schmitt, J. H. M. M., Robrade, J., Ness, J.-U., Favata, F., & Stelzer, B. 2005, *A&A*, 432, L35
- Smith, N., Bally, J., Shuping, R. Y., Morris, M., & Hayward, T. L. 2004, *ApJ*, 610, L117
- Smith, N., Bally, J., Shuping, R. Y., Morris, M., & Kassis, M. 2005, *AJ*, 130, 1763
- Stelzer, B., Flaccomio, E., Briggs, K., et al. 2007, *A&A*, 468, 463
- Stelzer, B. & Schmitt, J. H. M. M. 2004, *A&A*, 418, 687
- Tsuboi, Y., Koyama, K., Hamaguchi, K., et al. 2001, *ApJ*, 554, 734
- Tsujimoto, M., Kobayashi, N., & Tsuboi, Y. 2005, *AJ*, 130, 2212
- Werner, M. W., Roellig, T. L., Low, F. J., et al. 2004, *ApJS*, 154, 1
- Whitney, B. A., Wood, K., Bjorkman, J. E., & Cohen, M. 2003, *ApJ*, 598, 1079
- Wolk, S. J., Harnden, Jr., F. R., Flaccomio, E., et al. 2005, *ApJS*, 160, 423
- Zapata, L. A., Rodríguez, L. F., Kurtz, S. E., & O'Dell, C. R. 2004a, *AJ*, 127, 2252
- Zapata, L. A., Rodríguez, L. F., Kurtz, S. E., O'Dell, C. R., & Ho, P. T. P. 2004b, *ApJ*, 610, L121

Table 5: NIR photometry of Class 0/Ia candidates.

Seq.	COUP	RA(2000)	Dec(2000)	J	H	K	[3.6]	[4.5]	[5.8]	[8.0]
Num.	ID	[deg]	[deg]							
1		83.7093162	-5.3641575				13.014± 0.035		10.132± 0.035	8.291± 0.035
2		83.7313619	-5.2982484				13.274± 0.023		10.300± 0.027	8.404± 0.026
3	274	83.7777349	-5.3789530				12.110± 0.016	10.598± 0.011	9.607± 0.017	
4		83.7940632	-5.5850858				12.866± 0.017	11.137± 0.004	10.008± 0.024	8.840± 0.012
5		83.7956871	-5.3627791		14.957± 0.044	12.585± 0.031	10.526± 0.112	9.742± 0.029		
6		83.8000978	-5.3113336		16.336± 0.023	14.827± 0.132	11.844± 0.014	10.796± 0.007	9.787± 0.027	
7	484	83.8020643	-5.4105966	15.875± 0.084	15.340± 0.073	13.177± 0.026	10.877± 0.015	9.628± 0.011		
8		83.8111246	-5.2812258			15.111± 0.017	12.590± 0.018	11.482± 0.031		
9	696	83.8137692	-5.3580026		14.500± 0.010	12.203± 0.011	10.066± 0.020	9.103± 0.014		
10	702	83.8141265	-5.3262308				12.004± 0.015	10.355± 0.009	9.240± 0.017	
11	860	83.8211125	-5.3168295		15.237± 0.010	12.850± 0.009	10.468± 0.011	9.491± 0.008		
12	859	83.8212087	-5.3038593			14.637± 0.012	11.509± 0.021	10.260± 0.007	9.406± 0.047	
13		83.8255845	-5.3414585	15.114± 0.080	14.999± 0.016	12.804± 0.008	11.057± 0.033	10.204± 0.029		
14		83.8302403	-5.3200782		16.206± 0.014	13.911± 0.009	12.070± 0.043	11.151± 0.029		
15		83.8319297	-5.2961715				11.352± 0.037	10.191± 0.010	8.963± 0.048	
16	1048	83.8320314	-5.3249635		14.869± 0.009	12.378± 0.011	10.116± 0.011	9.337± 0.006		
17	1115	83.8362894	-5.3239664		15.173± 0.020	11.749± 0.015	8.577± 0.005	7.584± 0.003	6.545± 0.006	5.297± 0.027
18		83.8363643	-5.2232223				11.194± 0.009	10.227± 0.023	9.405± 0.024	8.388± 0.035
19	1197	83.8425168	-5.3355986			15.253± 0.047	11.508± 0.020	10.407± 0.011		
20		83.8479858	-5.4635150				13.088± 0.039		10.216± 0.044	8.384± 0.070
21	1321	83.8554596	-5.3351016				11.293± 0.022	10.118± 0.012	8.572± 0.116	
22		83.8634267	-5.4475646				11.977± 0.018		9.206± 0.039	7.573± 0.045
23		83.8997573	-5.3532412		16.440± 0.016	14.683± 0.011	12.755± 0.028	11.812± 0.023		

Table 6: NIR photometry of Class 0/Ib candidates.

Seq.	COUP	RA(2000)	Dec(2000)	J	H	K	[3.6]	[4.5]	[5.8]	[8.0]
Num.	ID	[deg]	[deg]							
24	103	83.7323261	-5.3363055		15.841± 0.016	13.369± 0.012	11.515± 0.007	10.718± 0.004	10.300± 0.030	
25		83.7545867	-5.3937160			14.382± 0.011	11.811± 0.005	11.018± 0.005	10.743± 0.017	
26	167	83.7570887	-5.4201451			15.427± 0.020	12.991± 0.014	12.173± 0.013	11.450± 0.036	
27	209	83.7672732	-5.3755507		15.475± 0.013	13.013± 0.016	10.755± 0.004	9.768± 0.003	9.082± 0.007	8.151± 0.018
28	407	83.7957359	-5.2559454	16.583± 0.043	12.803± 0.037	10.836± 0.032	9.232± 0.001	8.464± 0.004	8.104± 0.004	7.707± 0.033
29	420	83.7970836	-5.4106294		16.107± 0.023	12.677± 0.013	9.662± 0.008	8.171± 0.004	7.447± 0.014	
30	448	83.7993539	-5.3500809		12.617± 0.024	10.011± 0.011	7.644± 0.002	6.807± 0.001	6.127± 0.005	5.326± 0.012
31	472	83.8007853	-5.4156826		12.477± 0.009	10.698± 0.012	8.904± 0.003	8.157± 0.004	7.487± 0.013	6.636± 0.027
32		83.8058429	-5.3914514				8.621± 0.009	7.010± 0.007	5.956± 0.008	5.096± 0.035
33	548	83.8064706	-5.2960711		14.648± 0.009	11.908± 0.012	9.992± 0.002	9.181± 0.002	8.590± 0.010	7.577± 0.019
34	570	83.8071662	-5.3599724		12.897± 0.023	10.624± 0.012	8.404± 0.011	7.445± 0.010	6.960± 0.032	
35		83.8074223	-5.3944417				7.047± 0.005	5.170± 0.006	3.888± 0.004	2.994± 0.038
36	595	83.8079975	-5.4501972		15.196± 0.014	11.901± 0.021	9.232± 0.004	8.236± 0.001	7.752± 0.012	7.369± 0.032
37		83.8195534	-5.3125430			13.387± 0.046	9.792± 0.008	8.530± 0.002	7.756± 0.018	7.093± 0.042
38	1030	83.8307100	-5.4283582	17.377± 0.083	13.356± 0.022	10.409± 0.016	7.654± 0.002	6.779± 0.001	6.034± 0.009	5.266± 0.021
39	1054	83.8325174	-5.2597844		16.173± 0.059	12.783± 0.030	9.339± 0.002	8.100± 0.004	7.200± 0.002	6.411± 0.016
40	1094	83.8346095	-5.3326871		13.958± 0.014	11.398± 0.008	8.927± 0.005	8.073± 0.004	7.824± 0.032	
41	1170	83.8408440	-5.3354363		14.985± 0.016	12.799± 0.017	10.155± 0.006	9.281± 0.005	9.164± 0.110	
42	1188	83.8420775	-5.3160413		16.641± 0.021	13.638± 0.014	10.825± 0.016	9.652± 0.006	8.930± 0.047	
43	1364	83.8604067	-5.3218452		15.505± 0.018	12.678± 0.010	10.317± 0.008	9.364± 0.004	8.923± 0.032	
44	1480	83.8822676	-5.3556764		14.409± 0.018	11.755± 0.016	9.401± 0.004	8.554± 0.002	8.868± 0.032	
45	1565	83.9236385	-5.3374070			15.703± 0.019	12.773± 0.013	11.751± 0.008	11.234± 0.035	





Table 9: X-ray photometry of the Class 0/I candidates taken from Getman et al. (2005b). A description of the columns is given in Section 5.2.

Seq. Num.	COUP ID	NetCts	PSF Frac	Exp. (ks)	$\log N_H$ ( $\text{cm}^{-2}$ )	kT1 (keV)	$\log \text{EM1}$ ( $\text{cm}^{-3}$ )	$\log L_{h,c}$ ( $\text{erg s}^{-1}$ )	$\log L_{t,c}$ ( $\text{erg s}^{-1}$ )
3	274	176	0.86	762.20	$22.56 \pm 0.06$	$15.00 \pm 15.00$	$52.28 \pm 0.06$	29.28	29.42
7	484	54	0.86	783.40	$22.54 \pm 0.14$	$2.85 \pm 1.67$	$51.96 \pm 0.31$	28.67	29.00
9	696	27	0.87	825.80	$22.16 \pm 0.28$	$9.06 \pm 15.00$	$51.19 \pm 0.31$	28.19	28.38
10	702	79	0.86	801.10	$22.31 \pm 0.17$	$3.25 \pm 1.71$	$51.86 \pm 0.27$	28.63	28.93
11	860	185	0.87	792.20	$22.60 \pm 0.12$	$5.73 \pm 4.09$	$52.34 \pm 0.20$	29.27	29.49
12	859	481	0.87	751.60	$22.77 \pm 0.05$	$1.90 \pm 0.22$	$53.28 \pm 0.12$	29.78	30.24
16	1048	162	0.87	795.80	$22.68 \pm 0.08$	$2.98 \pm 0.84$	$52.51 \pm 0.19$	29.24	29.56
17	1115	27	0.86	794.00	$22.83 \pm 0.19$	$1.13 \pm 0.70$	$52.43 \pm 1.00$	28.56	29.37
19	1197	15	0.87	799.30	...	...	...	...	...
21	1321	184	0.87	714.40	$23.11 \pm 0.09$	$4.51 \pm 2.98$	$52.82 \pm 0.29$	29.69	29.94
24	103	58	0.87	783.40	$22.63 \pm 0.13$	$0.95 \pm 0.35$	$52.64 \pm 1.00$	28.61	29.60
26	167	88	0.86	739.20	$22.73 \pm 0.10$	$1.16 \pm 0.24$	$52.79 \pm 1.00$	28.94	29.72
27	209	97	0.87	824.10	$22.37 \pm 0.13$	$4.86 \pm 3.60$	$51.90 \pm 0.22$	28.80	29.03
28	407	479	0.87	737.40	$22.63 \pm 0.07$	$3.61 \pm 0.99$	$52.91 \pm 0.16$	29.71	30.00
29	420	65	0.86	838.20	$22.29 \pm 0.13$	$3.45 \pm 2.65$	$51.70 \pm 0.26$	28.48	28.78
30	448	2249	0.86	820.50	$22.52 \pm 0.02$	$2.24 \pm 0.12$	$53.64 \pm 0.05$	30.24	30.64
31	472	501	0.86	456.20	$22.55 \pm 0.05$	$2.80 \pm 0.38$	$53.18 \pm 0.10$	29.88	30.21
33	548	2315	0.87	774.50	$22.54 \pm 0.02$	$3.06 \pm 0.25$	$53.59 \pm 0.04$	30.33	30.65
34	570	4070	0.87	829.40	$22.64 \pm 0.02$	$3.35 \pm 0.22$	$53.86 \pm 0.03$	30.63	30.93
36	595	624	0.87	779.80	$22.69 \pm 0.04$	$2.31 \pm 0.18$	$53.23 \pm 0.10$	29.84	30.23
38	1030	3616	0.87	749.80	$22.98 \pm 0.02$	$15.00 \pm 1.00$	$53.89 \pm 0.03$	30.88	31.01
39	1054	1630	0.88	707.30	$22.64 \pm 0.02$	$2.59 \pm 0.25$	$53.62 \pm 0.07$	30.28	30.64
40	1094	214	0.87	801.10	$22.61 \pm 0.07$	$2.79 \pm 0.55$	$52.60 \pm 0.17$	29.30	29.64
41	1170	150	0.87	799.30	$22.61 \pm 0.08$	$1.03 \pm 0.22$	$52.96 \pm 1.00$	29.02	29.91
42	1188	232	0.87	686.10	$22.73 \pm 0.04$	$1.70 \pm 0.27$	$53.10 \pm 0.16$	29.54	30.05
43	1364	501	0.88	779.80	$22.70 \pm 0.03$	$4.30 \pm 1.02$	$52.94 \pm 0.11$	29.80	30.05
44	1480	914	0.86	684.40	$22.69 \pm 0.03$	$2.10 \pm 0.18$	$53.51 \pm 0.08$	30.07	30.50
45	1565	385	0.88	746.20	$22.52 \pm 0.05$	$2.50 \pm 0.40$	$52.85 \pm 0.12$	29.50	29.86

Table 10: Upper Limits of the X-ray undetected Class 0/I candidates. A description of the columns is given in Section 5.2.

Seq. Num.	RA (2000) (deg)	Dec (2000) (deg)	Cts hard	Cts tot.	Exp. (ks)	$\log L_{h,c}^1$ ( $\text{erg s}^{-1}$ )	$\log L_{h,c}^2$ ( $\text{erg s}^{-1}$ )	$\log L_{h,c}^3$ ( $\text{erg s}^{-1}$ )	$\log L_{t,c}^1$ ( $\text{erg s}^{-1}$ )	$\log L_{t,c}^2$ ( $\text{erg s}^{-1}$ )	$\log L_{t,c}^3$ ( $\text{erg s}^{-1}$ )
1	83.70931200	-5.36415800	26.38	32.58	710.29	28.44	28.27	28.76	28.84	29.44	29.65
2	83.73136100	-5.29824800	69.32	86.29	739.17	28.84	28.67	29.16	29.25	29.85	30.05
4	83.79406000	-5.58508600	661.04	3605.31	681.67	29.85	29.69	30.18	30.90	31.50	31.71
5	83.79568709	-5.36277907	18.18	31.25	817.28	28.21	28.05	28.54	28.76	29.36	29.57
6	83.80009500	-5.31133400	21.00	26.16	781.40	28.29	28.13	28.62	28.70	29.30	29.51
8	83.81112700	-5.28122600	30.07	64.72	632.86	28.54	28.38	28.87	29.19	29.79	30.00
13	83.82558451	-5.34145849	16.28	21.07	800.83	28.17	28.01	28.50	28.60	29.20	29.41
14	83.83023800	-5.32007800	19.08	22.96	782.92	28.25	28.09	28.58	28.65	29.25	29.45
15	83.83193200	-5.29617200	27.37	31.85	764.63	28.42	28.25	28.74	28.80	29.40	29.61
18	83.83636500	-5.22322200	2873.07	4004.38	698.35	30.48	30.31	30.80	30.94	31.54	31.75
20	83.84798400	-5.46351500	19.52	23.76	784.75	28.26	28.09	28.58	28.66	29.26	29.47
22	83.86342600	-5.44756500	16.24	20.93	732.72	28.21	28.04	28.53	28.63	29.23	29.44
23	83.89975700	-5.35324100	19.93	23.70	651.91	28.35	28.18	28.67	28.74	29.34	29.55
25	83.75458500	-5.39371600	14.13	18.14	762.24	28.16	27.94	28.37	28.56	29.15	29.36
32	83.80584286	-5.39145145	14.85	19.82	346.70	28.52	28.30	28.73	28.94	29.54	29.74
35	83.80742228	-5.39444168	14.63	22.59	336.57	28.53	28.31	28.74	29.01	29.60	29.81
37	83.81955700	-5.31254300	846.89	1300.70	780.42	29.92	29.71	30.14	30.40	31.00	31.21

Table 11: X-ray parameters of the Class II candidates. This table is available in its entirety in electronic form.

Seq. Num.	COUP ID	$\log N_H$ ( $\text{cm}^{-2}$ )	kT1 (keV)	log EM1 ( $\text{cm}^{-3}$ )	kT2 (keV)	log EM2 ( $\text{cm}^{-3}$ )	$\log L_{h,c}$ ( $\text{erg s}^{-1}$ )	$\log L_{t,c}$ ( $\text{erg s}^{-1}$ )
46	12	$21.33 \pm 0.18$	$14.34 \pm 11.68$	$52.44 \pm 0.05$	...	...	29.48	29.64
47	13	$20.00 \pm 2.12$	$12.58 \pm 15.00$	$51.51 \pm 0.17$	...	...	28.54	28.71
48	21	$20.79 \pm 2.06$	$0.68 \pm 0.11$	$51.63 \pm 0.17$	$1.77 \pm 0.47$	$51.89 \pm 0.12$	28.38	29.04
49	29	$21.59 \pm 0.03$	$0.81 \pm 0.06$	$52.56 \pm 0.13$	$3.13 \pm 0.32$	$52.82 \pm 0.03$	29.59	30.04
52	37	$20.00 \pm 2.34$	$0.67 \pm 0.33$	$51.13 \pm 0.63$	...	...	26.70	28.10
53	40	$20.35 \pm 2.00$	$0.86 \pm 0.11$	$51.55 \pm 0.15$	$6.29 \pm 4.63$	$51.64 \pm 0.08$	28.62	28.99
54	44	$21.79 \pm 0.32$	$1.14 \pm 0.35$	$51.50 \pm 0.29$	...	...	27.64	28.44
...								

Table 12: X-ray parameters of the Class III candidates. This table is available in its entirety in electronic form.

Seq. Num.	COUP ID	$\log N_H$ ( $\text{cm}^{-2}$ )	kT1 (keV)	log EM1 ( $\text{cm}^{-3}$ )	kT2 (keV)	log EM2 ( $\text{cm}^{-3}$ )	$\log L_{h,c}$ ( $\text{erg s}^{-1}$ )	$\log L_{t,c}$ ( $\text{erg s}^{-1}$ )
194	6	$20.67 \pm 0.43$	$0.85 \pm 0.12$	$52.17 \pm 0.11$	$4.37 \pm 0.95$	$52.62 \pm 0.04$	29.50	29.84
197	7	$21.12 \pm 0.12$	$0.78 \pm 0.09$	$52.16 \pm 0.12$	$2.32 \pm 0.27$	$52.68 \pm 0.04$	29.32	29.79
201	9	$20.93 \pm 0.04$	$0.83 \pm 0.01$	$53.58 \pm 0.02$	$2.30 \pm 0.08$	$53.94 \pm 0.01$	30.57	31.08
202	10	$21.37 \pm 0.03$	$0.83 \pm 0.02$	$53.59 \pm 0.03$	$3.04 \pm 0.11$	$53.87 \pm 0.01$	30.64	31.08
203	14	$20.00 \pm 1.21$	$0.74 \pm 0.13$	$51.42 \pm 0.21$	...	...	27.11	28.39
205	20	$20.81 \pm 0.14$	$0.69 \pm 6.24$	$51.64 \pm 1.00$	$9.23 \pm 15.00$	$51.19 \pm 0.21$	28.25	28.82
...								

Table 13: Upper Limits of the X-ray undetected Class II and III candidates

Seq. Num.	ID H97	RA (2000) (deg)	Dec (2000) (deg)	Cts hard	Cts tot.	Exp. (ks)	$\log L_{h,c}^1$ (erg s <sup>-1</sup> )	$\log L_{h,c}^2$ (erg s <sup>-1</sup> )	$\log L_{h,c}^3$ (erg s <sup>-1</sup> )	$\log L_{t,c}^1$ (erg s <sup>-1</sup> )	$\log L_{t,c}^2$ (erg s <sup>-1</sup> )	$\log L_{t,c}^3$ (erg s <sup>-1</sup> )	Class
51	85	83.69498179	-5.35801543	117	130	0.76	28.83	27.89	29.10	28.73	28.54	29.38	II
55	108	83.70820425	-5.31230548	83	66	0.45	28.92	27.99	29.19	28.66	28.47	29.31	II
66	179	83.74109068	-5.47828377	79	237	0.73	28.67	27.73	28.94	29.00	28.81	29.66	II
74	219	83.75862700	-5.30628963	27	35	0.77	28.19	27.26	28.46	28.15	27.96	28.81	II
98	294	83.77694276	-5.51927167	32	39	0.71	28.29	27.35	28.56	28.23	28.04	28.89	II
113	402	83.80437902	-5.56763586	57	66	0.66	28.58	27.64	28.85	28.50	28.31	29.15	II
123	449	83.81012490	-5.55521463	51	500	0.68	28.51	27.57	28.78	29.36	29.17	30.01	II
153	682	83.83838625	-5.55481843	47	57	0.71	28.46	27.52	28.73	28.40	28.21	29.05	II
166	789	83.85709585	-5.49312187	24	29	0.76	28.14	27.20	28.41	28.08	27.89	28.73	II
339	729	83.84592814	-5.49483049	23.07	28.00	0.72	28.12	27.21	28.41	27.92	27.85	28.77	III
210	62	83.67848933	-5.42114559	38.07	55.00	0.75	28.31	27.40	28.60	28.19	28.12	29.04	III

Table 14: Literature Class 0/I counterparts.

Seq. Num.	Class	COUP	LMH00	MLLA02	SBS04	SBS04 name	SBS05	RBP05
1	0/Ia							
2	0/Ia							
3	0/Ia	274						
4	0/Ia							
5	0/Ia		TPSC 63	771				
6	0/Ia							
7	0/Ia	484	TPSC 50					
8	0/Ia							
9	0/Ia	696	TPSC 59					
10	0/Ia	702						
11	0/Ia	860						
12	0/Ia	859						
13	0/Ia		TPSC 56	950				
14	0/Ia							
15	0/Ia							
16	0/Ia	1048						
17	0/Ia	1115						
18	0/Ia							
19	0/Ia	1197		988				
20	0/Ia							
21	0/Ia	1321		991				
22	0/Ia							
23	0/Ia							
24	0/Ib	103						
25	0/Ib							
26	0/Ib	167						
27	0/Ib	209						
28	0/Ib	407						
29	0/Ib	420	TPSC 74					MAX 18
30	0/Ib	448	TPSC 65					MAX 22
31	0/Ib	472	TPSC 31					
32	0/Ib		TPSC 3	369	10	134-330	7	MAX 40
33	0/Ib	548						
34	0/Ib	570	TPSC 35	797				MAX 44
35	0/Ib		TPSC 78		1	138-340	16	MAX 46
36	0/Ib	595						
37	0/Ib							
38	0/Ib	1030	TPSC 41					
39	0/Ib	1054						
40	0/Ib	1094	TPSC 73	1001				
41	0/Ib	1170	TPSC 44	990				
42	0/Ib	1188						
43	0/Ib	1364						
44	0/Ib	1480						
45	0/Ib	1565						